

## ABSTRACT

Classification of Human Head Motion Patterns using Creeping Wave Propagations

Drew G. Bresnahan, M.S.E.C.E.

Mentor: Yang Li, Ph.D.

Wearable electronics are continually being developed for a multitude of applications like remote health monitoring, personal activity tracking, and gaming. To design efficient wireless communication between multiple on-body devices, propagation models of the human body must be considered. Due to the creeping wave effect of radio waves near a curved surface, the human body itself acts as a channel capable of supporting and affecting wireless signals. The around-head creeping wave propagation behavior of three different frequencies has been investigated. Since these continuous frequency signals are affected by the movements of the human body, their altered signatures are also classifiable as effects of distinct daily activities like eating, drinking, breathing, and speaking. To improve the measurement system for practical operation in the field, the network analyzer is replaced with smaller, cheaper sensor alternatives including narrowband and wideband candidates.

Classification of Human Head Motion Patterns using Creeping Wave Propagations

by

Drew G. Bresnahan, B.S.E.C.E.

A Thesis

Approved by the Department of Electrical and Computer Engineering

---

Kwang Lee, Ph.D., Chairperson

Submitted to the Graduate Faculty of  
Baylor University in Partial Fulfillment of the  
Requirements for the Degree of

Master of Science in Electrical and Computer Engineering

Approved by the Thesis Committee

---

Yang Li, Ph.D., Chairperson

---

Scott Koziol, Ph.D.

---

Rachel Eike, Ph.D.

Accepted by the Graduate School

May 2018

---

J. Larry Lyon, Ph.D., Dean

Copyright © 2018 by Drew G. Bresnahan

All rights reserved

## TABLE OF CONTENTS

CHAPTER ONE .....	1
Introduction .....	1
<i>Background and Motivation</i> .....	1
<i>Content Structure of This Thesis</i> .....	4
CHAPTER TWO .....	6
Narrowband Propagation Study with Unmoving Test Subjects.....	6
<i>Measurement</i> .....	6
<i>Full-wave Simulations</i> .....	12
<i>Wave Mode Analysis</i> .....	15
<i>Theoretical Model</i> .....	18
<i>Conclusion</i> .....	20
CHAPTER THREE .....	21
Narrowband Signal Distortion Classification with Moving Test Subjects .....	21
<i>Background Information</i> .....	21
<i>Dynamic Neck Measurement</i> .....	22
<i>Neural Network Background</i> .....	25
<i>Activity Classification using Convolutional Neural Network</i> .....	28
<i>Conclusion</i> .....	31
CHAPTER FOUR.....	32
Measurement of Around-Body Creeping Waves Using Wearable Sensor Modules ....	32
<i>Introduction</i> .....	32
<i>VNA Baseline Measurements</i> .....	33
<i>Digi XBee Modules</i> .....	36
<i>Time Domain PulsON Modules</i> .....	39
<i>Conclusion</i> .....	42
CHAPTER FIVE .....	43
Conclusion.....	43
<i>Summary</i> .....	43
<i>Future Work</i> .....	44
BIBLIOGRAPHY .....	45

## LIST OF FIGURES

Fig. 1. Concept diagram of wireless body area network.....	2
Fig. 2. Creeping wave illustration.....	3
Fig. 3. Antenna characteristics: (a) picture of $\frac{1}{4}$ -wavelength bridge monopole matched at 2.45 GHz, (b) return loss when antenna is placed near the forehead, (c) return loss when antenna is placed near the neck. ....	7
Fig. 4. Measurement paths around the head and neck. ....	8
Fig. 5. Measurement setup: (a) A bridge monopole antenna, (b) around horizontal path, (c) around vertical path, (d) around neck path.....	8
Fig. 6. Horizontal head scan S21 data: (a) 433 MHz monopole transmission loss (dB), (b) 915 MHz monopole transmission loss, (c) 2.45 GHz monopole transmission loss, (d) 433 MHz monopole phase delay (degrees), (e) 915 MHz monopole phase delay, (f) 2.45 GHz monopole phase delay. ....	10
Fig. 7. Vertical head scan S21 data: (a) 433 MHz monopole transmission loss (dB), (b) 915 MHz monopole transmission loss, (c) 2.45 GHz monopole transmission loss, (d) 433 MHz monopole phase delay (degrees), (e) 915 MHz monopole phase delay, (f) 2.45 GHz monopole phase delay. ....	10
Fig. 8. Neck scan S21 data: (a) 433 MHz monopole transmission loss (dB), (b) 915 MHz monopole transmission loss, (c) 2.45 GHz monopole transmission loss, (d) 433 MHz monopole phase delay (degrees), (e) 915 MHz monopole phase delay, (f) 2.45 GHz monopole phase delay. ....	11
Fig. 9. 2.45 GHz S21 data for: (a) Horizontal head magnitude, (b) vertical head magnitude, (c) neck magnitude, (d) horizontal head phase, (e) vertical head phase, and (f) neck phase.....	12
Fig. 10. (a) Simplified simulation model. (b) Realistic simulation model. ....	13
Fig. 11. Simulation results compared to measurements for the horizontal head scan for (a) 433 MHz, (b) 915 MHz, (c) 2.45 GHz, for the vertical head scan for	

(d) 433 MHz, (e) 915 MHz, (f) 2.45 GHz, and for the neck scan for (g) 433 MHz, (h) 915 MHz, (i) 2.45 GHz. ....	14
Fig. 12. ESPRIT parameter extraction results plotted for the horizontal head path. ....	16
Fig. 13. ESPRIT parameter extraction results plotted for the vertical head path. ....	16
Fig. 14. ESPRIT parameter extraction results plotted for the neck path. ....	17
Fig. 15. Reconstruction using extracted dominant wave mode parameters for (a) horizontal head scan magnitude, (b) vertical head magnitude, (c) neck magnitude, (d) horizontal head phase, (e) vertical head phase, and (f) neck phase. ....	18
Fig. 16. Theory curve compared to measurements and simplified FEKO simulations, horizontal head scan: (a) 433 MHz; (b) 915 MHz; (c) 2.45 GHz. ....	19
Fig. 17. Theory curve compared to measurements and simplified FEKO simulations, vertical head scan: (a) 433 MHz; (b) 915 MHz; (c) 2.45 GHz. ....	19
Fig. 18. Examples of male and female S21 parameters across the neck measured at 2.45 GHz for the four different activities: (a) chewing, (b) swallowing, (c) breathing, and (d) speaking. ....	24
Fig. 19. Neural network concept diagram. ....	26
Fig. 20. Convolutional neural network concept diagram. Picture taken from MathWorks [23]. ....	27
Fig. 21. Illustration of how a local receptive field is connected to a single hidden layer neuron. Picture taken from MathWorks [23]. ....	27
Fig. 22. Spectrograms generated from S21 parameter of (a) chewing, (b) drinking, (c) breathing, and (d) speaking. ....	28
Fig. 23. Architecture of CNN used to classify neck-related activity spectrograms. ....	29
Fig. 24. CNN validation accuracy vs spectrogram window width for (a) the first scenario, and (b) the second scenario. ....	30
Fig. 25. Narrowband around-neck creeping wave measurement. ....	34
Fig. 26. S21 magnitude curves due to (a) chewing, (b) drinking, (c) deep breathing, and (d) speaking. ....	34

Fig. 27. Wideband around-head creeping wave measurement. ....	35
Fig. 28. (a) VNA scan of frequency from 3 to 5 GHz. (b) Time domain representation of UWB frequency scan. ....	36
Fig. 29. XBees with antennas attached to test subject’s neck.....	37
Fig. 30. Measured signal strength in dBm between on-neck antennas for chewing compared between XBees and VNA. ....	37
Fig. 31. XBee attachment setup for front of torso—back is similar. ....	38
Fig. 32. Measured signal strength in dBm between on-torso antennas for single arm swinging compared between XBees and VNA. ....	39
Fig. 33. Time Domain PulsON radar modules with antennas attached with long cables. ....	40
Fig. 34. . Comparison of around-head channel impulse response between PulsON radars and VNA scan. ....	40
Fig. 35. Antennas attached to front and back of test subject torso. ....	41
Fig. 36. Comparison of around-torso channel impulse response between PulsON radars and VNA scan. ....	41

## LIST OF TABLES

Table 1. List of Test Subject Traits.....	23
Table 2. Confusion Matrix for CNN Training.....	30

## PUBLICATIONS

### Journal Articles

- [1] **D. Bresnahan**, Y. Li, Y. Kim, S. Koziol, “Monitoring human head and neck-based motions from dynamic around-neck creeping wave propagations,” submitted for publication.
- [2] **D. Bresnahan** and Y. Li, “Investigation of creeping wave propagation around the human head at ISM frequencies,” *IEEE Antennas Wireless Propag. Lett.*, vol. 16, pp. 2767-2770, Aug 2017.

### Conference Papers

- [3] **D. Bresnahan** and Y. Li, “Measurement of around-body creeping waves using wearable sensor modules,” submitted for publication.
- [4] **D. Bresnahan** and Y. Li, “Classification of human head motion patterns using transmission coefficient of on-neck antennas,” *UNSC-URSI National Radio Science Meeting*, Boulder, CO, Jan 2018.
- [5] **D. Bresnahan** and Y. Li, “Measurement, simulation, and theory of creeping wave propagations around the human head at 2.45 GHz.” in *Proc. Texas Symp. Wireless Microwave Circuits Systems (WMCS)*, Waco, TX, 2017, pp. 14-17.
- [6] **D. Bresnahan** and Y. Li, “Investigation of creeping wave propagations around the human head and neck at ISM frequency bands,” *UNSC-URSI National Radio Science Meeting*, Boulder, CO, Jan 2017.

## ACKNOWLEDGMENTS

I would like to thank my advisor, Dr. Yang Li, for his guidance and mentorship. I would also like to thank Dong Xue and Bin Xu for their advice and participation. Lastly, I would like to thank Baylor Scott and White Health and the National Science Foundation (ECCS-1609371) for their financial sponsorship of this work.

## DEDICATION

To my mother and father, whose love and support never wavers

## CHAPTER ONE

### Introduction

#### *Background and Motivation*

A wireless body-area network (WBAN) can be defined as a group of wirelessly interconnected sensors meant to be worn on the human body to measure a physical quantity or provide a function. Most examples of WBANs are medical in nature, remotely monitoring physiological effects in or on the body. Wearable consumer electronics like the Fitbit® or smart watches which send information to the user's smartphone can also be considered WBAN nodes. With the recent advancements in wireless communication and miniaturization of electronics, the future may hold many WBAN applications for functions that we can only imagine today. Fig. 1 shows a basic concept diagram of a WBAN. While WBAN nodes can be any type of sensor, like accelerometers or thermometers, this work will focus on antennas which radiate radio frequency (RF) electromagnetic waves near the surface of the human body.

Monitoring and tracking human motion patterns during daily activities is an important problem with interesting applications, including remote health monitoring [1], [2], athletic training [3], and computer gaming [4]. A substantial amount of research has been conducted to track compound motions like walking, running, hopping, and sitting [5]-[7], which all involve movement of the human torso and limbs. Lately, small-scale movements over specific regions of the human body, such as mouth movements or finger motions, have also attracted the attention of researchers [8]-[11]. The head-neck region of

the body hosts important physiological processes like speaking, eating, and breathing; therefore, this region holds great potential for localized activity classification.

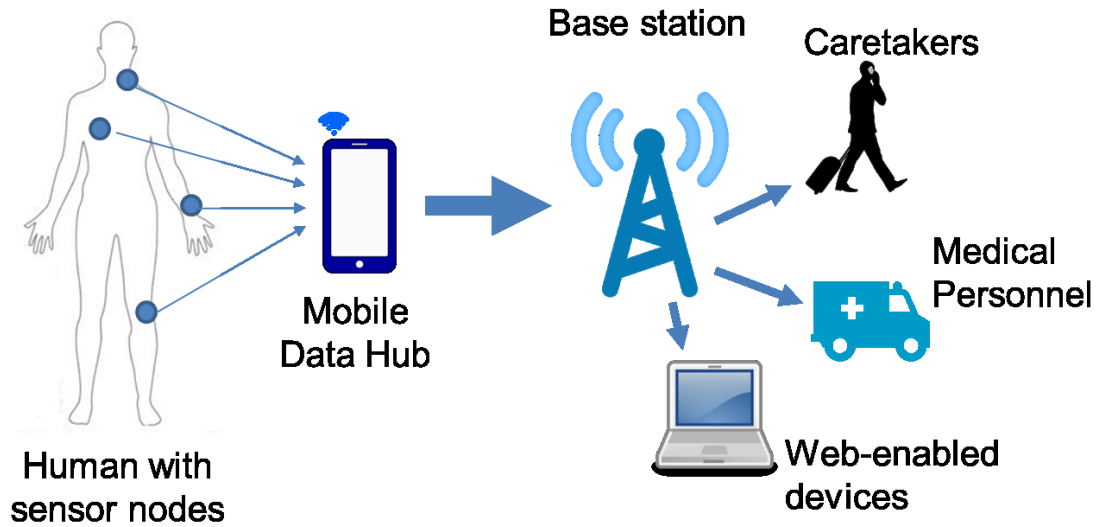


Fig. 1. Concept diagram of wireless body area network.

Previous works have suggested several creative approaches for tracking these types of activities: Yatani and Truong [8] investigated acoustics as a method of classifying neck-related activities (e.g. eating and drinking) by developing a wearable microphone prototype sensor. They were able to achieve 79.5% classification accuracy using a support vector machine algorithm. Cheng *et al.* [9] studied the ability of wearable capacitive sensors to recognize various physiological signs like heartbeat and breathing. Fang *et al.* [10] developed a radio-based wearable prototype system that is capable of tracking head-related activities (e.g. coughing, eating, drinking, and speaking). Their approach eliminates the need of using a microphone or camera, and it achieves a higher classification accuracy of 86.3% using principal component analysis on the fine-grained channel state information extracted from the system.

Because the nodes of a WBAN communicate wirelessly, it is imperative to understand the behavior of the electromagnetic wave propagations that take place near the human body surface. Previous works have investigated the line-of-sight and non-line-of-sight wave propagations along the human torso, providing insight into how different paths of communication may operate for two on-body nodes [12]-[15]. However, the head and neck region of the human body has yet to be fully modeled for propagation path loss and phase delay between two transceivers.

The creeping wave phenomenon [16] is the dominant theory describing the main propagation mechanism of radio waves travelling around curved portions of the body. Creeping waves are illustrated in Fig. 2, where one can see how an incident wave front will diffract and spread into the shadowed space behind the target, effectively travelling around the curved path while attenuating. Although it was popularized by engineers investigating phantom returns in radar applications [17], the creeping wave phenomenon is significantly observable when a source radiates near the many curves and contours of the human body.

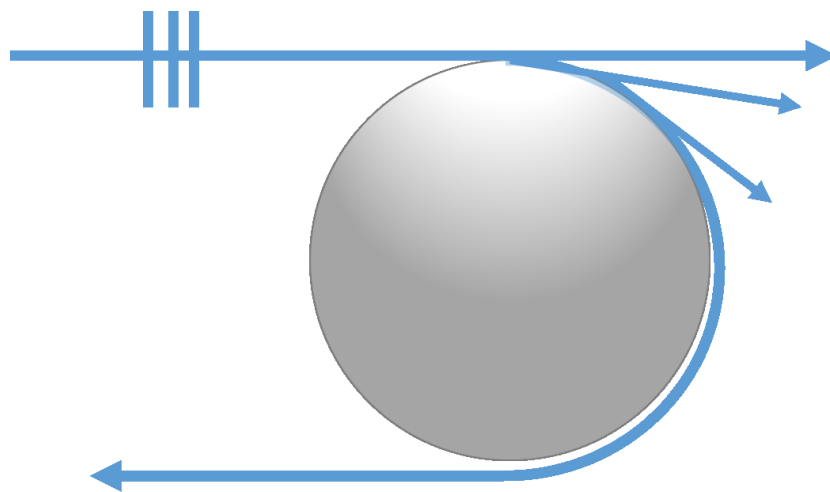


Fig. 2. Creeping wave illustration.

## *Content Structure of This Thesis*

In this work, the primary goal is to use creeping wave propagations around the human head and neck to classify different head and neck-related activities such as eating, drinking, breathing, and speaking. In order to accomplish this, the following objectives are accomplished.

### *Chapter Two*

Creeping wave propagations around unmoving human test subjects' heads are first investigated through direct measurements, simulations, and verifying with a theoretical model. Magnitude decay and phase delay of three different ISM-band frequencies are considered: 433 MHz, 915 MHz, and 2.45 GHz.

### *Chapter Three*

2.45 GHz creeping wave signals are measured around the neck of six test subjects as they act out different activities. The motions of the throat and jaw disturb the radio channel around the neck, affecting the measured S-parameters of two neck-worn antennas. Spectrograms of the different S-parameter disturbance patterns are used to train a convolutional neural network to classify the activities based on their time-frequency radio signatures.

### *Chapter Four*

Two different kinds of small, affordable sensors are used to replace the vector network analyzer as the measurement device in on-body wave propagation tests. The two sensors feature narrowband and wideband measurement schemes, respectively. The

removal of the network analyzer from the measurement system is crucial for any practical future use of WBANs in everyday life.

## CHAPTER TWO

### Narrowband Propagation Study with Unmoving Test Subjects

#### *Measurement*

To begin, a single frequency wireless signal is considered as it propagates around the human head. Three separate wireless signals with frequencies of 433 MHz, 915 MHz, and 2.45 GHz are launched near the unmoving (static) human head. These frequencies are selected since they are centered within the Industrial, Scientific, and Medical (ISM) spectrum bands. The type of antenna used to generate the waves is a quarter-wavelength “bridge” monopole, as shown in Fig. 3(a). Three pairs of antennas are created to support the three different frequencies. The antenna wire lengths are 17.32 cm, 8.20 cm, and 3.06 cm with square top ground plane sizes of  $4 \times 4 \text{ cm}^2$ ,  $2 \times 2 \text{ cm}^2$ , and  $2 \times 2 \text{ cm}^2$ , corresponding to center resonant frequencies at 433 MHz, 915 MHz, and 2.45 GHz, respectively. The ground plane is fabricated in a “bridge” shape to allow the 90-degree SMA adapter to fit below the antenna and remain flush with the human head surface.

Two monopole antennas are connected to port 1 and 2 of an Agilent PNA-L N5230C Network Analyzer (VNA). All three pairs of monopole antennas are well matched ( $S_{11} < -10 \text{ dB}$ ) at their designed frequencies of 433 MHz, 915 MHz, and 2.45 GHz when placed on the subject’s forehead. The  $S_{11}$  parameter of the 2.45 GHz antennas when placed near the body is shown in Fig. 3(b)-(c), which both indicate a good impedance match. The gains of each antenna are measured to be close to 5 dBi in an open

space environment. To ensure on-body wave mechanisms can be strongly excited, the monopoles are oriented orthogonally to the human head surface [18].

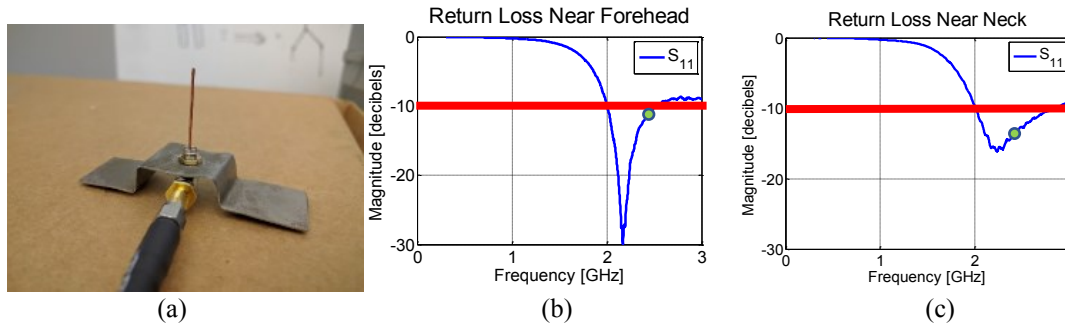


Fig. 3. Antenna characteristics: (a) picture of  $\frac{1}{4}$ -wavelength bridge monopole matched at 2.45 GHz, (b) return loss when antenna is placed near the forehead, (c) return loss when antenna is placed near the neck.

Three paths are chosen for measurement, as show in Fig. 4: a  $360^\circ$  horizontal head path, a  $180^\circ$  vertical head path, and a  $360^\circ$  horizontal neck path. The transmitting antenna is placed on the side of the head just above the ear, and the receiving antenna is moved around the head in 1.5 cm increments while the VNA measures the S-parameters for each sample location.

S-parameters, short for Scattering parameters, describe the behavior of a linear electrical network as it is stimulated by a steady state electrical signal. The  $S_{11}$  parameter is proportional to the amount of energy sent from port 1 that is reflected back into port 1 due to load impedance mismatch. The  $S_{21}$  parameter is proportional to the energy sent from port 1 to port 2, which in this setup is the creeping wave signal strength between the antennas.

Fig. 5(a)-(c) shows the experimental setup for each of the three path scans. These experiments were conducted in a spacious, indoor hallway with the test subject standing upright and still. The results presented below are from one female test subject, age 27 years, with horizontal head circumference of 53 cm, vertical head circumference of 57

cm, and neck circumference of 30 cm. All presented measurement results are from this test subject unless otherwise specified.

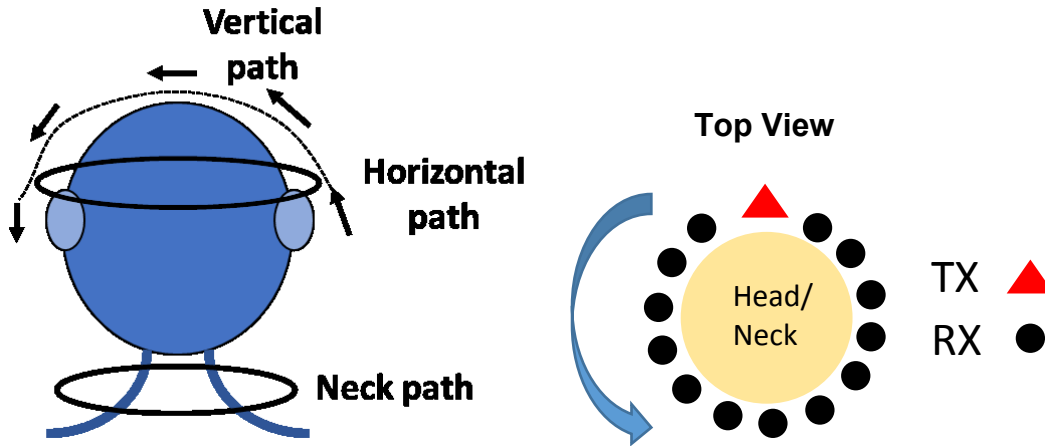


Fig. 4. Measurement paths around the head and neck.

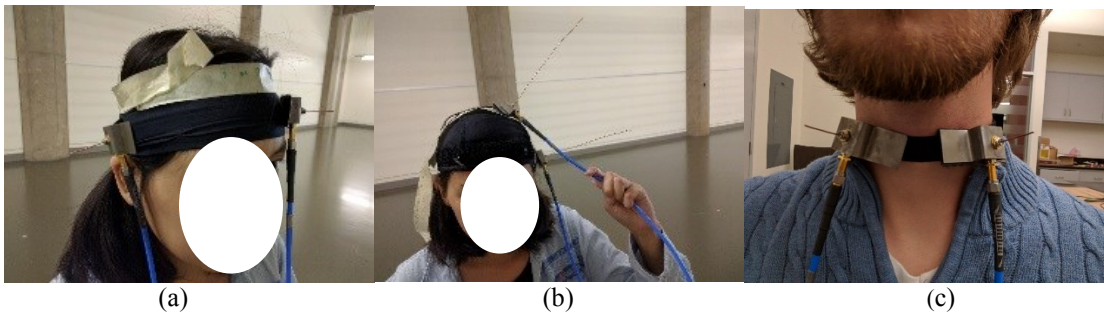


Fig. 5. Measurement setup: (a) around horizontal path, (b) around vertical path, (c) around neck path.

Fig. 6 shows the horizontal head  $S_{21}$  magnitude on dB scale and phase on degree scale. The vertical axis corresponds to distance between the antennas along the head path and the horizontal axis corresponds to frequency swept from 300 MHz to 3 GHz on the VNA for each sample point. The center resonant frequencies of the antennas are obvious as the regions of strongest magnitude. For example, the 915 MHz scan in Fig. 6(b) has a strong, red, vertically stretching region centered near the 1 GHz mark, where the 915 MHz antenna pair would radiate and receive the most energy. The same observation can

be made with the 433 MHz and 2.45 GHz plots. A noticeable symmetry exists across the middle horizontal line through each of the graphs, indicating that the creeping wave experiences nearly identical exponential magnitude decay and linear phase delay along either direction of the horizontal head path. For a fixed frequency, the signal magnitude drops as the distance increases, then increases slightly near the 24-cm mark ( $180^\circ$  from the transmitting antenna), then increases to the initial level as the receiving antenna is moved back next to the transmitting antenna, resulting in the symmetrical pattern in the plots.

Fig. 7 shows the measured  $S_{21}$  against frequency and distance between the antennas along the vertical path. These magnitude and phase plots are similar to those in Fig. 6, but they lack the vertical symmetry of the horizontal head path plots since the measured path is only along the top of the head from ear to ear, covering  $180^\circ$  instead of  $360^\circ$ . Since the neck would block the antennas from completely traversing the vertical  $360^\circ$  loop, only the  $180^\circ$  path is considered. The phase delay of both horizontal and vertical scans appears rather linear, indicating there may only be one dominant wave mode along those paths.

Fig. 8 displays similar magnitude and phase results for the horizontal neck scan. The symmetry of each plot is once again apparent, due to the symmetry of the human neck. However, notice that for each frequency the magnitude decays more quickly than that of either head scan. Discussion of this phenomenon follows.

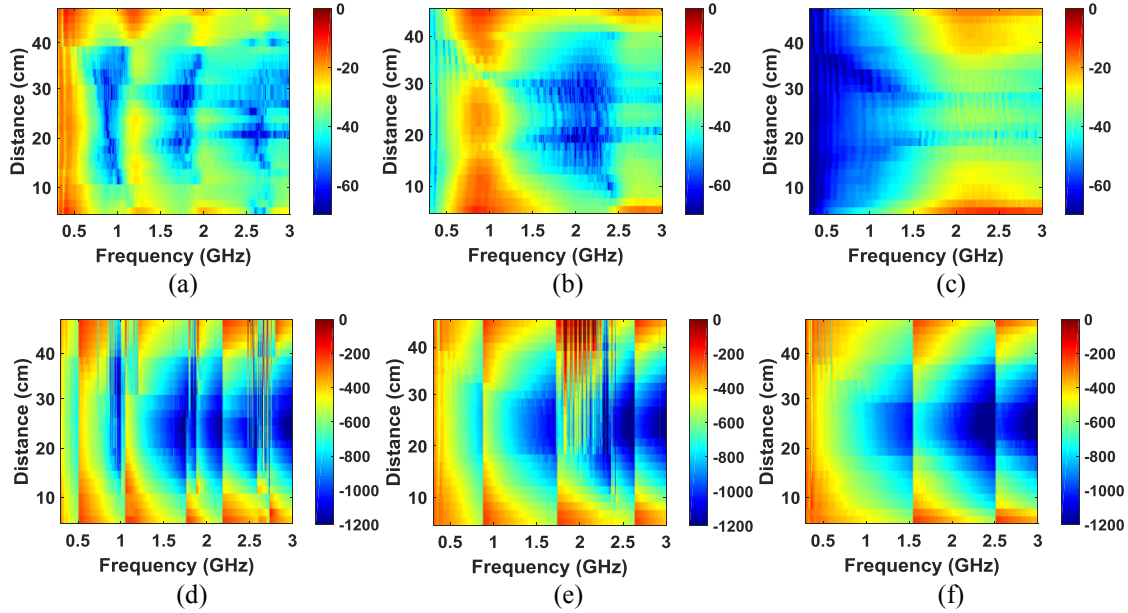


Fig. 6. Horizontal head scan S21 data: (a) 433 MHz monopole transmission loss (dB), (b) 915 MHz monopole transmission loss, (c) 2.45 GHz monopole transmission loss, (d) 433 MHz monopole phase delay (degrees), (e) 915 MHz monopole phase delay, (f) 2.45 GHz monopole phase delay.

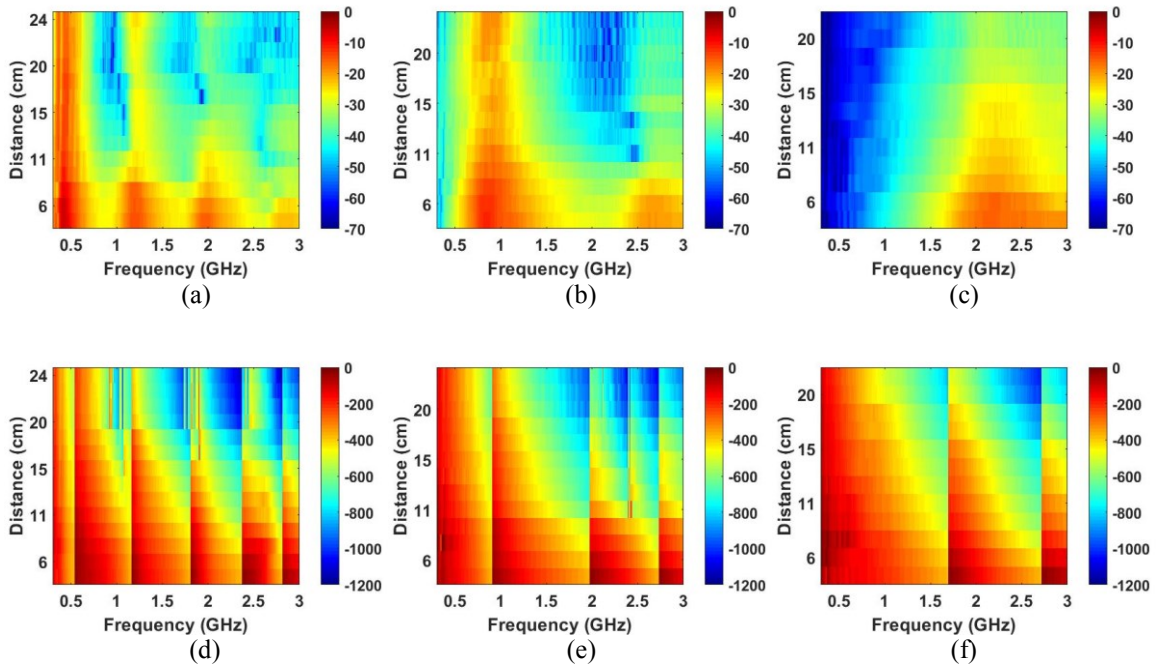


Fig. 7. Vertical head scan S21 data: (a) 433 MHz monopole transmission loss (dB), (b) 915 MHz monopole transmission loss, (c) 2.45 GHz monopole transmission loss, (d) 433 MHz monopole phase delay (degrees), (e) 915 MHz monopole phase delay, (f) 2.45 GHz monopole phase delay.

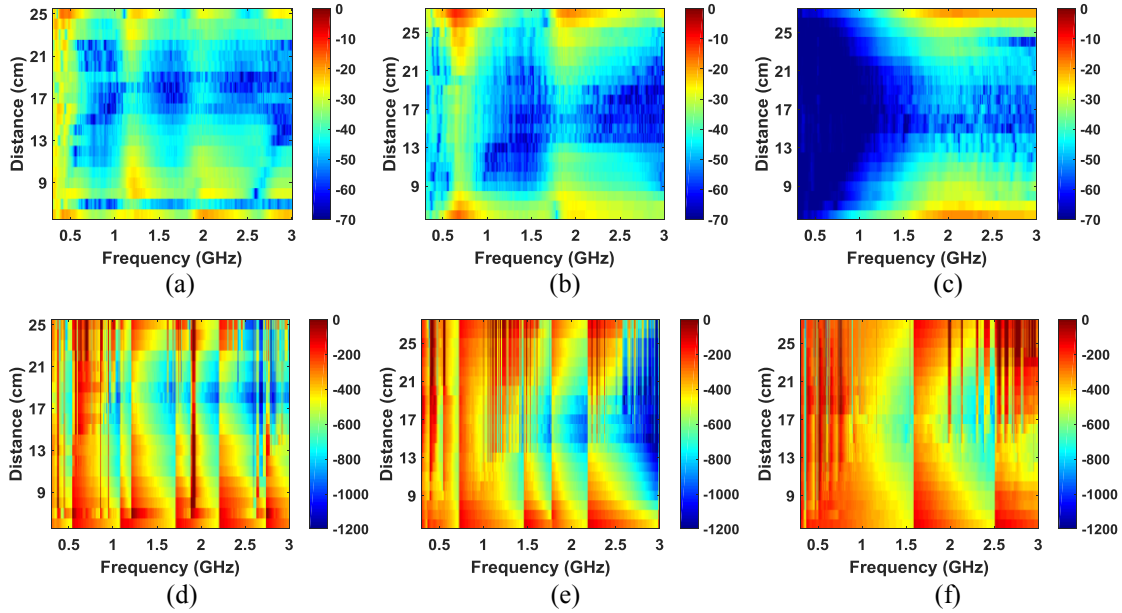


Fig. 8. Neck scan S21 data: (a) 433 MHz monopole transmission loss (dB), (b) 915 MHz monopole transmission loss, (c) 2.45 GHz monopole transmission loss, (d) 433 MHz monopole phase delay (degrees), (e) 915 MHz monopole phase delay, (f) 2.45 GHz monopole phase delay.

By selecting a single frequency at the horizontal axis of any plot from Figs. 6-8 and examining the changes of the signal along the distance axis, it becomes simple to visualize how that frequency component propagates along the three head paths. For this section, an additional male test subject is measured using the same testing procedure as before. Shown in Fig. 9(a), the 2.45 GHz  $S_{21}$  curve attenuates exponentially, increases for a short distance at the middle of the path distance, decreases once more, then finally exponentially increases as the receiving antenna is brought near the transmitting antenna.

Because of the circular nature of this measurement path, it is rather obvious that the signal strength will start high, attenuate to low, and return to high as the antennas are separated and brought closer together. However, it is important to recognize that due to the symmetric nature of the plots in Fig. 9(a),(c), there are two dominant wave modes propagating around the horizontal head path. If this were not true, the signal would not increase back to the initial level as the receiver antenna moves along its forward path.

Since the measurement path is a circle, it is concluded that there are two primary wave modes, one propagating in the clockwise direction, and the other in the counter-clockwise direction. The irregularities in  $S_{21}$  at the middle of the path indicates that there is constructive and destructive interference between these wave fronts. The image in Fig. 10 illustrates how these two symmetric wave modes are intuitively understandable due to the shape of the head and the radiation pattern of the monopole antennas used for testing. The vertical head scan shown below in Fig. 9(b),(e) does not exhibit the symmetrical “W-shaped” pattern, since only the 180° path was measured.

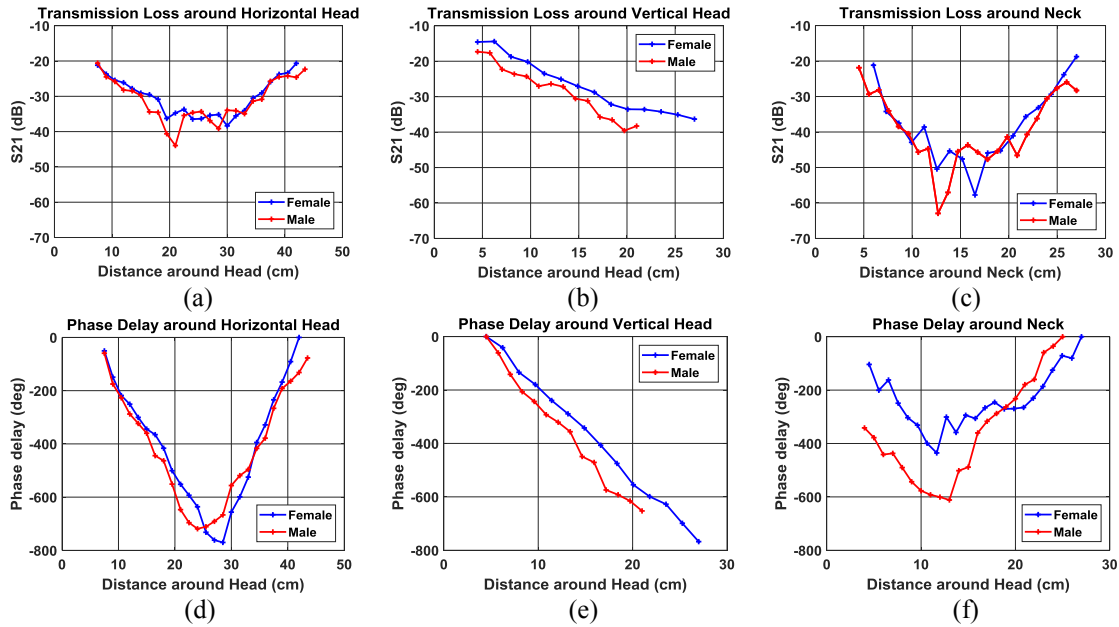


Fig. 9. 2.45 GHz  $S_{21}$  data for: (a) Horizontal head magnitude, (b) vertical head magnitude, (c) neck magnitude, (d) horizontal head phase, (e) vertical head phase, and (f) neck phase.

### Full-wave Simulations

To verify the measurements, full-wave simulations are performed for the horizontal head, vertical head, and neck path using the FEKO simulation software [19]. Two simulation models were considered for this study: a homogeneous, geometrically simplified model shown in Fig. 10(a), and an inhomogeneous, geometrically realistic

phantom model shown in Fig. 10(b). The realistic model is not easily scalable to the shape and dimensions of the human test subjects, hence the inclusion of the simplified model which is easy to scale and modify.

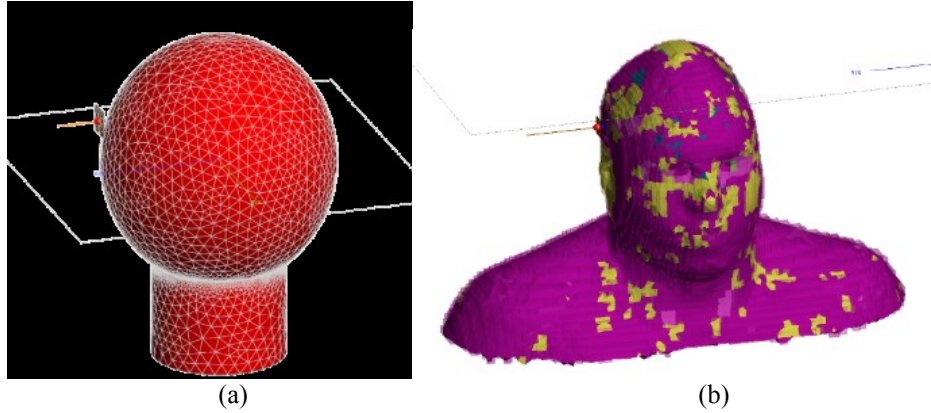


Fig. 10. (a) Simplified simulation model. (b) Realistic simulation model.

The simplified head model consists of a spheroid representing the head and a cylinder representing the neck, which are both filled with dielectric material equivalent to  $2/3$  of muscle tissue relative permittivity and conductivity (e.g., 52.7 and 1.7 S/m at 2.45 GHz) and are scaled to the head size of the test subject. The use of the  $2/3$  muscle tissue approximation is a common estimation used by many other biomedical studies to simplify the model and shorten simulation time [20], [21]. The inhomogeneous, realistic head model represents a more accurate description of the human head. However, its size cannot be scaled to the test subject, and it takes a much longer time to simulate for high mesh densities. The mesh discretization applied in the simulation is 12 segments per wavelength.

Fig. 11 shows the results of the 2.45 GHz horizontal head simulation plotted on the same axis as the measurement data for the same setup. One can observe decent agreement between all curves. The realistic simulation data is the most comparable to the measurement results for Fig. 11(b),(c), but the simplified simulation curve is closer to the

measurements in Fig. 11(a). Fig. 11(d)-(f) show similar plots for the vertical head scan, and Fig. 11(g)-(i) show the simulation plots for the neck scan.

Since the results of the simplified model align with the measurements, it is not necessary to always use the realistic model. A homogeneous approximation of a human is good enough for creeping wave simulation.

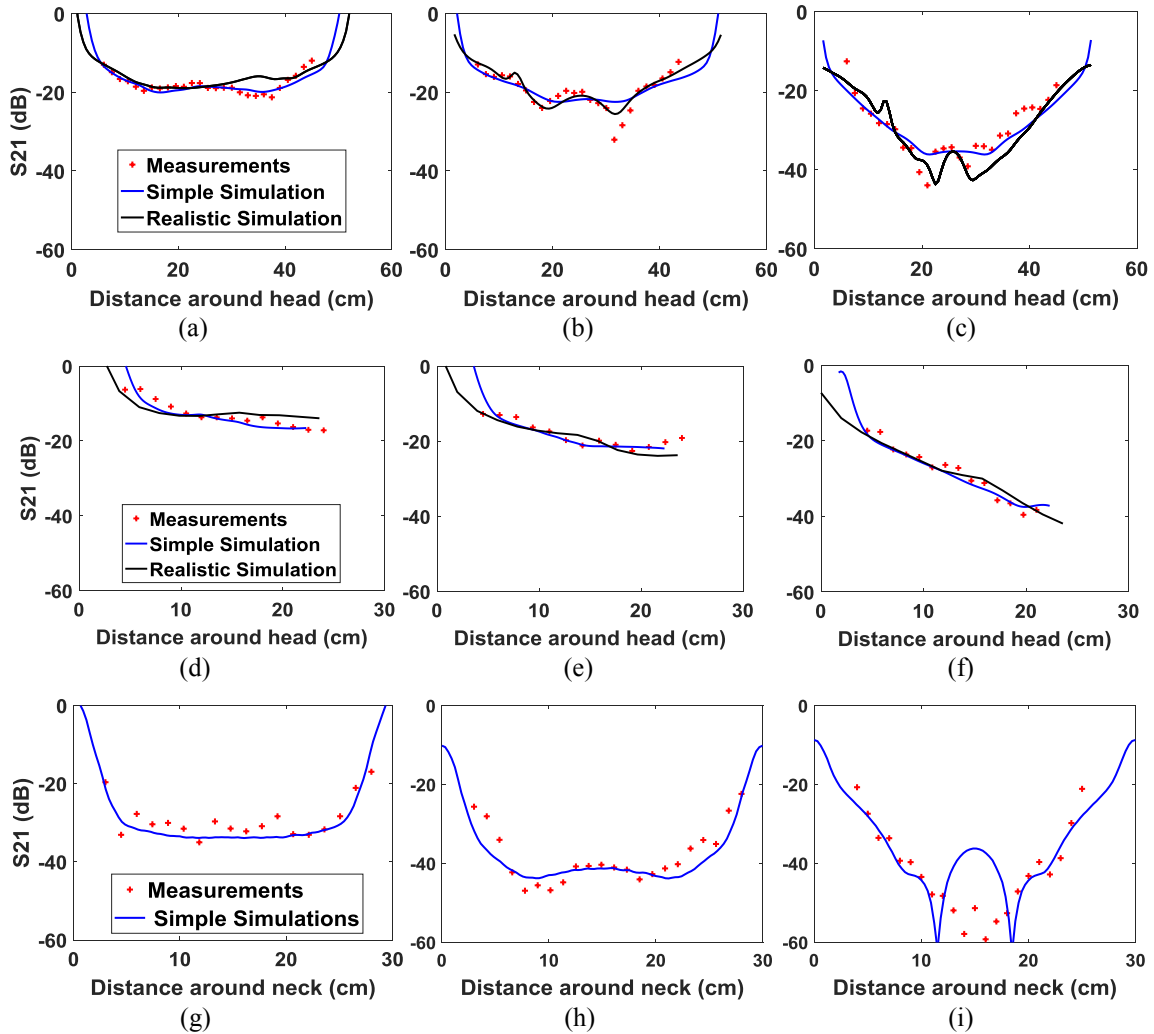


Fig. 11. Simulation results compared to measurements for the horizontal head scan for (a) 433 MHz, (b) 915 MHz, (c) 2.45 GHz, for the vertical head scan for (d) 433 MHz, (e) 915 MHz, (f) 2.45 GHz, and for the neck scan for (g) 433 MHz, (h) 915 MHz, (i) 2.45 GHz.

### Wave Mode Analysis

To provide more physical insights into the above results, we next model the measured  $S_{21}$  into a summation of  $N$  propagating modes, in the form

$$S_{21}(d, f) \cong \sum_{n=1}^N c_n(f) e^{-j\beta_n(f)d} e^{-\alpha_n(f)d}. \quad (1)$$

Each mode is associated with a unique mode magnitude  $c_n$ , phase constant  $\beta_n$ , and attenuation constant  $\alpha_n$ . The ESPRIT algorithm (Estimation of Signal Parameters via Rotational Invariance Technique) [22] is applied to extract the mode parameters. Implementing ESPRIT with Matlab, it is possible to visualize the wave modes that comprise the observed patterns discussed in the sections above. By plotting the extracted phase constant and magnitude from each of the four most prominent wave modes, an image like that of Fig. 12 is generated. Two distinct tracks are visible, indicating that out of the four strongest modes, only two are non-negligible. These correspond to the clockwise and counter-clockwise wave fronts propagating in either direction around the horizontal head path. The absolute values of the phase constants (“Beta”) increase with frequency, as expected. Since the tracks appear rather linear, it is reasonable to claim that the horizontal head path channel experiences little to no frequency dispersion.

Like Fig. 12, Fig. 13 shows the wave parameter extraction results plotted for the vertical head scan path. The first 2 dominant modes are plotted, however only one primary mode appears, since the measurement path only covered the top of the head and the neck masks the creeping wave from propagating in both directions like in the horizontal head path case. Fig. 14 displays similar results for the neck scan path. The

neck is decidedly noisier than the other two scans, most likely due to the presence of the chin, chest, head, and hair near the scan path.

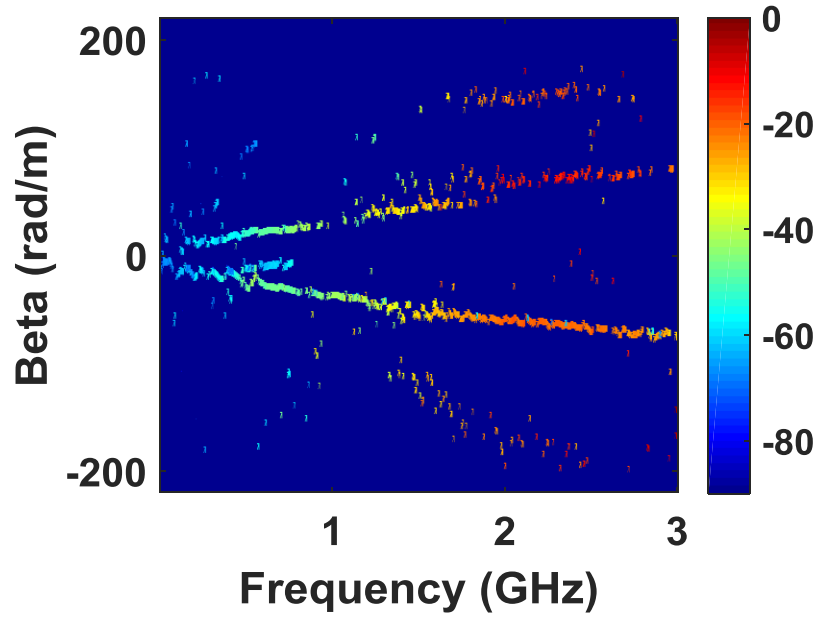


Fig. 12. ESPRIT parameter extraction results plotted for the horizontal head path.

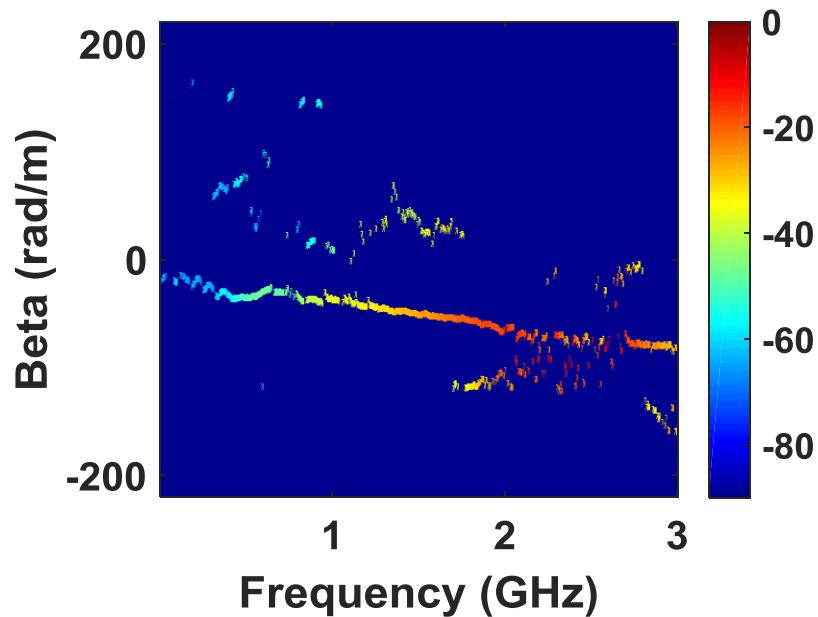


Fig. 13. ESPRIT parameter extraction results plotted for the vertical head path.

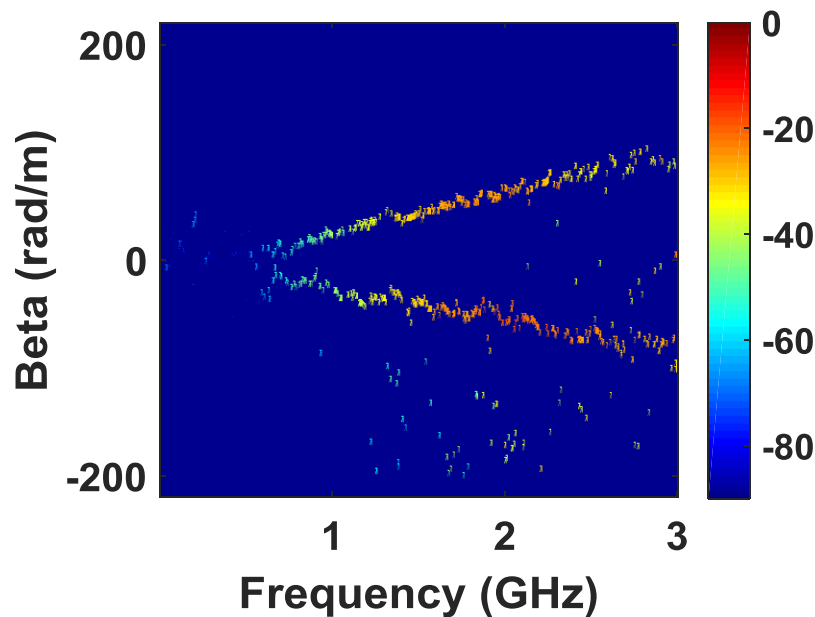


Fig. 14. ESPRIT parameter extraction results plotted for the neck path.

To verify the data presented in Figs. 12-14, the two dominant modes' (one mode in the vertical head case) parameters are used to generate a curve which is compared to the raw measurement data in Fig. 15. Decent alignment between both data sets in each case confirms that there are two dominant modes for the horizontal head and neck paths, and one dominant mode for the vertical path. Due to the unclean data collected around the neck, the addition of only two modes were not sufficient to closely reconstruct the original measurement curves. A closer fit between the curves can be found by increasing the number of modes used in the reconstruction. This applies in all cases.

For each path scan at any certain frequency, it appears that the wavenumber is slightly greater than the wavenumber for a wave in free space at the same respective frequency. This implies that the creeping waves propagate slower than the speed of light in a vacuum. This may be explained by the proximity to the human flesh, where its dielectric properties slow a portion of the electric fields that cross from air into the head.

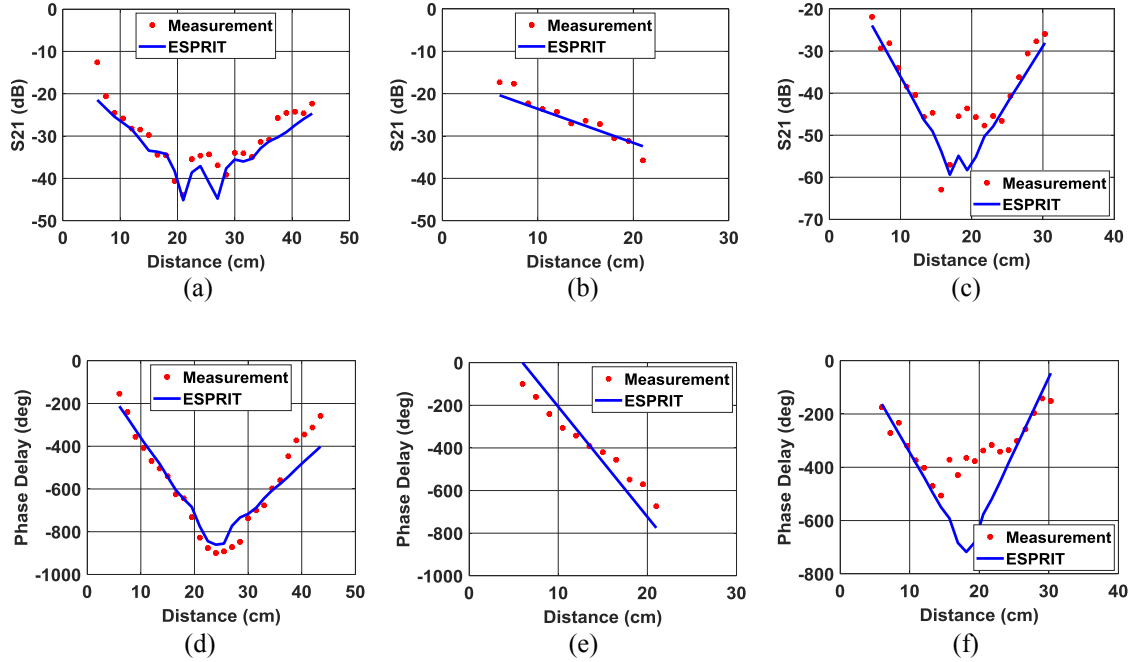


Fig. 15. Reconstruction using extracted dominant wave mode parameters for (a) horizontal head scan magnitude, (b) vertical head magnitude, (c) neck magnitude, (d) horizontal head phase, (e) vertical head phase, and (f) neck phase.

### Theoretical Model

The creeping wave theory developed by Alves *et al* [18] is introduced to compare with the previously discussed simulation and measurement results. The following equation represents the transmission loss between transmitting and receiving antennas, where  $G$  is the transmission strength from transmitting to receiving antenna;  $c$  is the speed of light in a vacuum;  $t_o^1$  is an empirical constant given in [18];  $G_{TX}$  and  $G_{RX}$  are the respective gains of the transmitting and receiving antennas;  $d$  is the circumferential distance around the head path;  $f$  is the operating frequency;  $a$  is the radius of the head; and  $p$  is the total circumference of the head:

$$G = \frac{\frac{10}{6} \pi^{\frac{4}{3}}}{4\pi^2 |t_1^0|^2} G_{TX} G_{RX} \frac{1}{d} \frac{1}{f^{\frac{10}{6}}} \frac{1}{a^{\frac{2}{3}}} \left| \left[ e^{-\alpha d} e^{-jkd} + e^{-\alpha(p-d)} e^{-jk(p-d)} \right]^2 \right| \quad (2)$$

The theoretical attenuation constant  $\alpha$  is given as follows. It is seen that  $\alpha$  is inversely proportional to the wavelength  $\lambda$  and radius  $a$ , implying the creeping wave experiences larger decay at higher frequency and smaller radius. Both phenomena have been observed in our measurement data.

$$\alpha_{dB/cm} = K \frac{f_{MHz}^{1/3}}{a_{cm}^{2/3}} \quad (3)$$

In Fig. 16 and Fig. 17 there are similar trends between the theoretical curve and the curves of the prior results. The theory curve best aligns with simulation and measurement at 2.45 GHz, since this case best complies with the condition from [18] that  $\lambda \ll p$ . However, lower frequencies of the theory model still show alignment with the measurements and simulations.

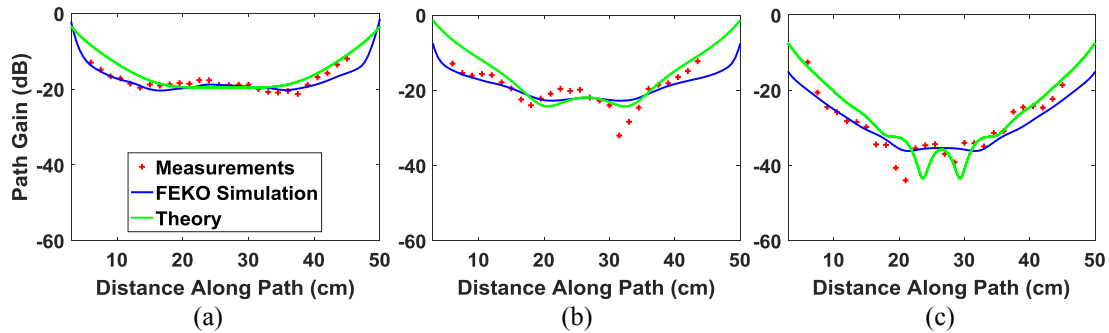


Fig. 16. Theory curve compared to measurements and simplified FEKO simulations, horizontal head scan: (a) 433 MHz; (b) 915 MHz; (c) 2.45 GHz.

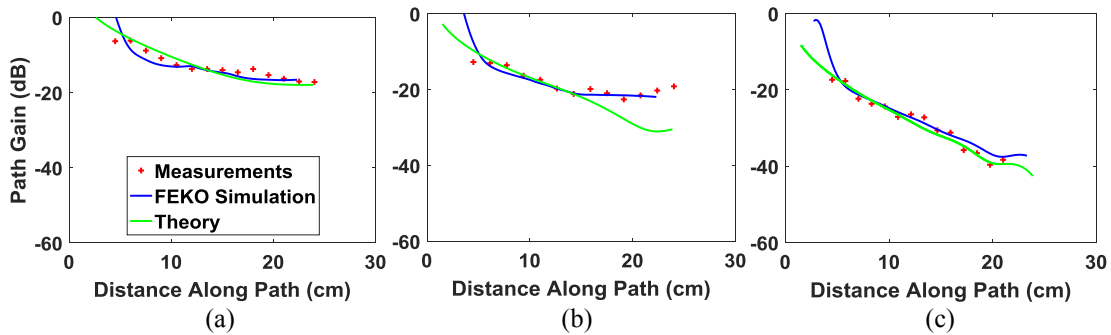


Fig. 17. Theory curve compared to measurements and simplified FEKO simulations, vertical head scan: (a) 433 MHz; (b) 915 MHz; (c) 2.45 GHz.

### *Conclusion*

In this chapter, measurements of around-head and around-neck narrowband creeping waves were conducted for 433 MHz, 915 MHz, and 2.45 GHz. Simulations and a theoretical model were used to verify and compare with the measurements. The ESPIRT algorithm was used to model the measured patterns as a summation of complex exponential terms to determine the dominant wave modes for each creeping wave path.

The radius of the creeping wave path curvature is a significant factor in the attenuation of the creeping wave signal—a smaller radius will cause greater attenuation of the signal. Higher operation frequency will also cause greater attenuation in the creeping wave. The phase delay of a creeping wave signal primarily depends on the distance from transmitter to receiver along the body path.

## CHAPTER THREE

### Narrowband Signal Distortion Classification with Moving Test Subjects

#### *Background Information*

Studies in the realm of computer body interfaces and WBAN systems have discovered the potential of using radio waves as a means of detecting different human body activities. In a manner similar to how Doppler radar can classify different weather patterns, so too can radio or microwave frequency signals be used as a sensing method for different human motion patterns. This has been shown in the works of Fang *et al* [10] who developed a wearable radio sensor system capable of classifying head-related activities (like eating and speaking) with 86.3% accuracy, and Xu *et al* [11] who was able to use the reflection coefficient of an antenna to monitor the movements of a subject's hand with over 90% accuracy.

The near environment surrounding an antenna directly affects the antenna's impedance characteristics. If a narrowband antenna is resonant at a certain frequency in free space, placing the antenna near or inside of a material with a high electric permittivity or conductivity will undoubtedly shift its resonant frequency. Using the equation

$$\beta = \frac{2\pi}{\lambda} = \omega\sqrt{\mu\varepsilon} , \quad (4)$$

it is clear that the steady-state wavelength  $\lambda$  of a signal with angular frequency  $\omega$  is inversely proportional to the square root of the permittivity  $\varepsilon$ . The magnetic permeability

$$\mu = \mu_r \mu_0 \quad (5)$$

is generally equal to  $\mu_0$ , the permeability of free space, and is therefore not a critical point of consideration for most nonmagnetic natural materials, including human tissue.

However, the lossless permittivity of a material is generally greater than that of free space, and is given as

$$\varepsilon = \varepsilon_r \varepsilon_0 \quad (6)$$

where  $\varepsilon_r$  is the relative permittivity (also referred to as a dielectric constant) and  $\varepsilon_0$  is the permittivity of free space. Most natural materials have  $\varepsilon_r > 1$ . If the conductivity of the material is greater than 0, then the permittivity can be expressed as a complex number,

$$\varepsilon = \varepsilon' - j \frac{\sigma}{\omega} \quad (7)$$

where  $\varepsilon'$  is the lossless permittivity defined in (6).

Equation (4) implies that as a material with sufficiently high permittivity or conductivity is brought near an antenna, the steady-state wavelength will increase in length, creating a downward shift in the antenna's resonant frequency. Effectively, the electrical dimensions of the antenna become longer as the dielectric material is brought near the source of radiation. If this principle is applied to a dielectric human body interacting with sensitive narrowband antennas, the resulting resonant frequency shifts and S-parameter fluctuations are potential tools to measure different motion patterns.

### *Dynamic Neck Measurement*

As humans undergo different daily activities, the RF channel around the neck is primarily influenced by movements of the head, shoulders, and surrounding neck tissue. When experiencing common body functions like eating or speaking, these channel

disturbances can form patterns in the measured S-parameters, which can be used to classify many different neck-related activities. For this study, we consider six test subjects acting out four different activities: *chewing*, *swallowing*, *breathing*, and *speaking*.

The dynamic (i.e. moving human) measurement setup is like the setup described in chapter 2, but now both the transmitting and receiving monopoles are kept stationary and 80° apart on the neck for the duration of the experiment. Table 1 lists the physical characteristics of the six test subjects. The network analyzer measured the 2.45 GHz S-parameters between the antennas for 20 seconds, sampling at 200 Hz. IF bandwidth of the VNA was set to 500 Hz. Each test subject repeated four trials of each of the four activities. Fig. 18 shows the magnitude (left) and phase (right) of the  $S_{21}$  parameter of test subjects “Male 1” and “Female 1” for the four separate activities.

Table 1. List of Test Subject Traits.

	Male 1	Male 2	Male 3	Male 4	Female 1	Female 2
Height (cm)	188	178	170	164	163	170
Weight (kg)	70	84	64	95	50	66
Circumference of Neck (cm)	36	40	36	42	30	34
Age (years)	22	27	35	42	27	26

It is clear from Fig. 18 that the four activities cause distinctly different S-parameter patterns in the time domain which can be used to distinguish them from one another. For example, the chewing (Fig. 18(a)) exhibits quick, sudden peaks and valleys as the chin of the test subject abruptly moves up and down. In contrast, the deep breathing (Fig. 18(c)) shows a slow, smooth rise and fall as the chest expands and affects the environment of the neck antennas. The swallowing (Fig. 18(b)) has a unique

repeating shape that distinguishes it from the other activities, whereas the speaking (Fig. 18(d)) is random, sporadic, and does not seem to follow a trend like the other activities.

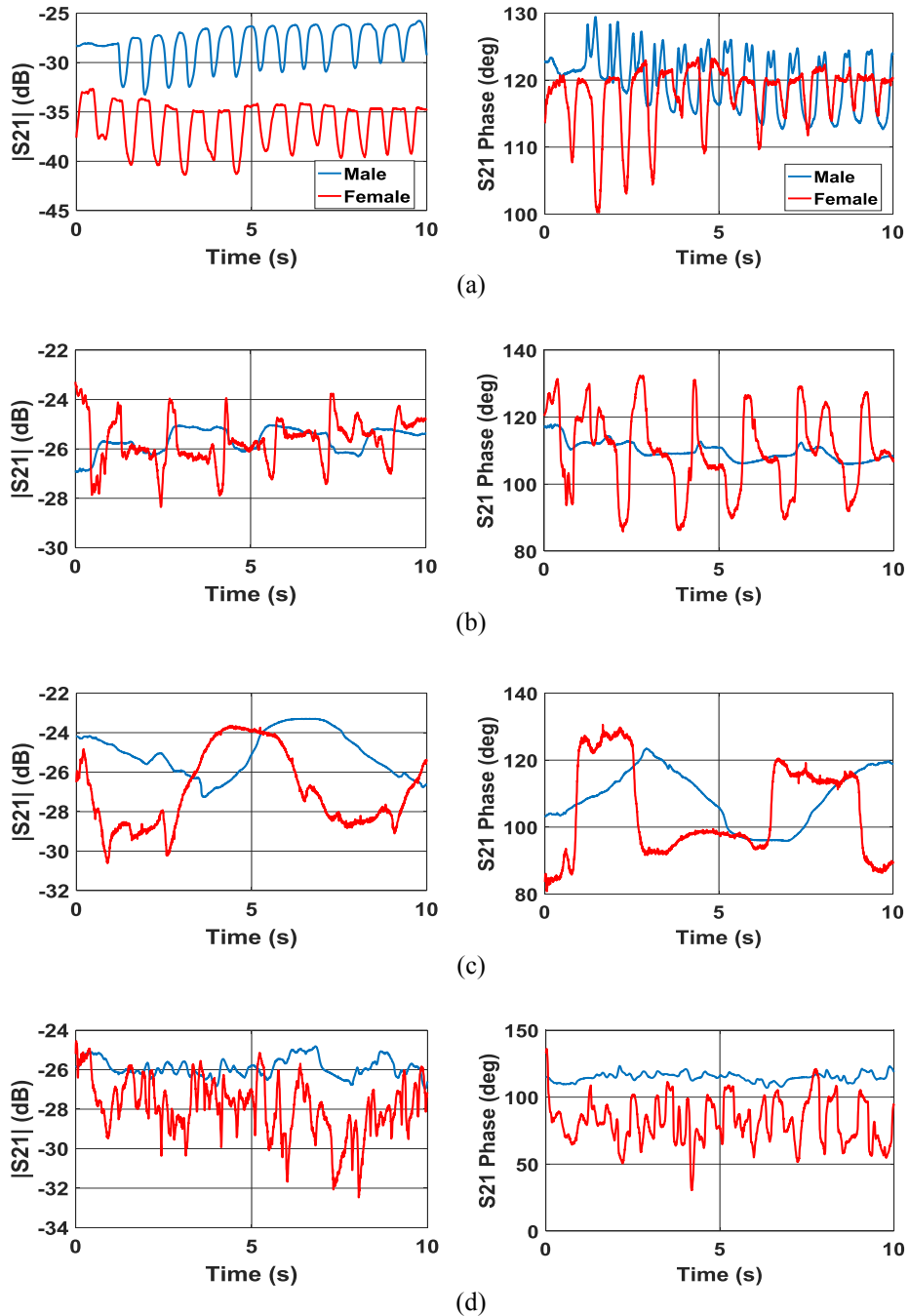


Fig. 18. Examples of male and female S21 parameters across the neck measured at 2.45 GHz for the four different activities: (a) chewing, (b) swallowing, (c) breathing, and (d) speaking.

The amplitude range of both the magnitude and the phase also may help differentiate the activities. Observe how the Male 1 chewing spans 5 dB of magnitude and 10 degrees of phase, compared to the Male 1 drinking which only spans 1-2 dB and 5 degrees. Although all the plotted activities were made intentionally periodic, actions like chewing and breathing are inherently periodic, implying the frequency domain contains rich information that may also prove useful when classifying head-related activities.

If enough diverse instances of these data were displayed here, the reader may be able to identify the activity of an unlabeled plot simply by recognizing the unique patterns appearing in each type of activity. This idea can extend to computer algorithms.

### *Neural Network Background*

A neural network is a computer algorithm capable of learning to generate an output based on given inputs by adjusting the weights and biases of its hidden neural connections. A neural network must be trained by an outside entity capable of labelling the input data as it presents it to the network. As more and more training data is presented to the network, the weights and biases are adjusted according to a gradient descent minimization of the *cost function*, which is a measure of how incorrect the network's answers are for each training iteration. The details of how neural networks learn are not covered here, but an excellent learning source is [23]. Once the training period is over and enough diverse input data have been presented to the network, the network performance is validated by submitting similar input data and evaluating if the outputs are correct or not. The number of correct outputs divided by the total number of answers (correct and incorrect) gives the percentage accuracy of the neural network.

Fig. 19 shows a concept diagram of a neural network. A “deep” neural network implies there are many hidden layers. This is a rather arbitrary distinction, with there being no hard requirement to be called “deep.” Each hidden layer corresponds to another layer of complexity the network can resolve in a problem (e.g. identifying edges or shapes in images instead of individual pixels). This architecture, called a *multilayer perceptron*, was devised decades ago and is considered insufficient for many applications today. There have been extensions to this concept that have become common solutions for image recognition, natural speech processing, and website advertisement optimization.

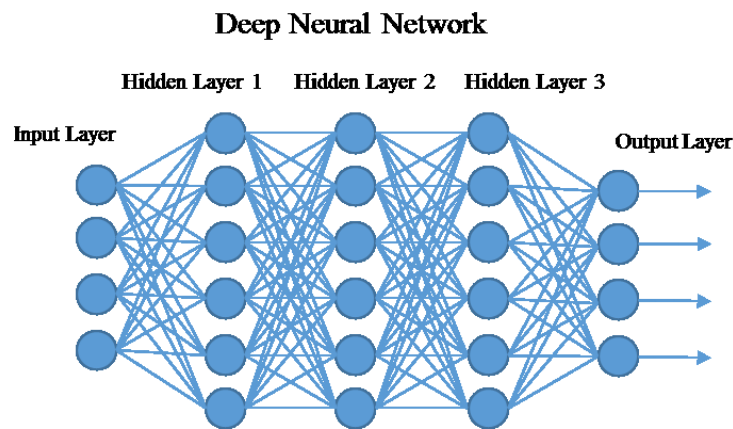


Fig. 19. Neural network concept diagram.

One of the extensions of the multilayer perceptron is called a convolutional neural network (CNN), which is illustrated in Fig. 20. A CNN connects sub-regions of the 2-dimensional input, called local receptive fields, to different hidden layer neurons as shown in Fig. 21. A 2-dimensional convolution is an efficient way to achieve this, hence the name of the architecture. The hidden layer identifies features in the previous layer through an *activation function*, which decides which neurons to “turn on” in the hidden layer. The hidden layer neural connections share identical weights and biases so that

features can be recognized regardless of where they are in the image. The result is then condensed into a pooling layer, which takes the average value of the activated neurons in a sub-region of the previous layer and stores it in one neuron. This immensely reduces the dimensionality of the problem by shrinking the number of parameters that the network needs to learn. After this process repeats through the multiple hidden layers, the fully-connected layer connects every neuron from the last hidden layer to the output neurons to combine the features and classify the image. The output is then produced like the answer to a multiple-choice test question. Note that if the CNN is presented with an image that it was never trained to recognize, it will confidently give an answer that is nowhere near correct. The network can only give answers for categories that it was trained for.

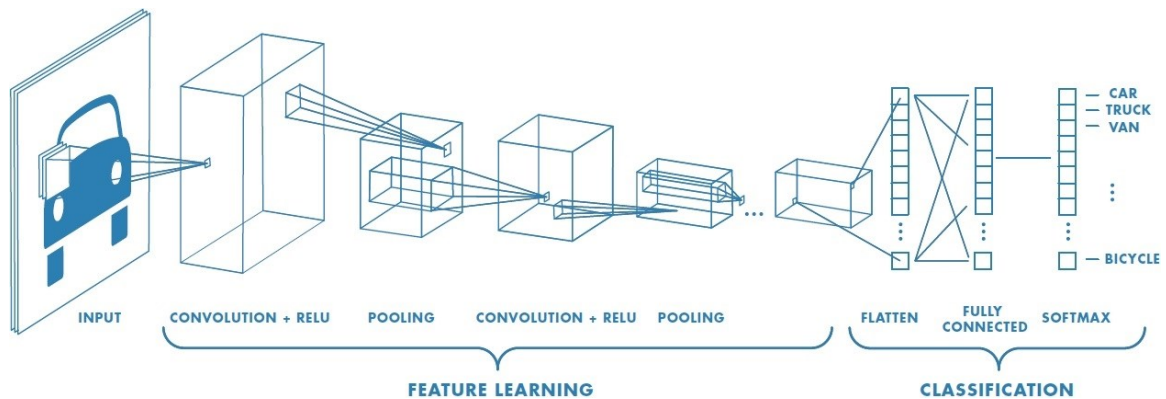


Fig. 20. Convolutional neural network concept diagram. Picture taken from MathWorks [23].

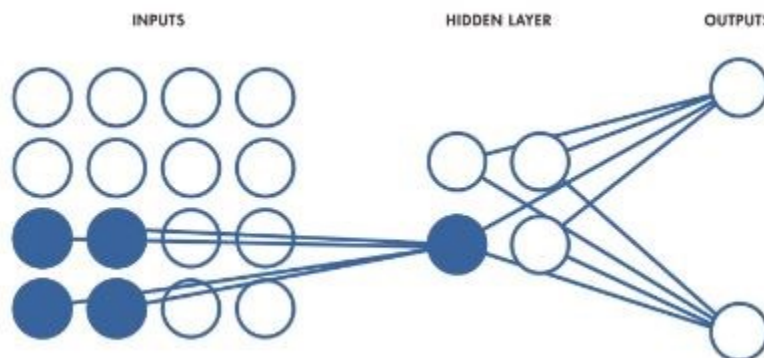


Fig. 21. Illustration of how a local receptive field is connected to a single hidden layer neuron. Picture taken from MathWorks [23].

### *Activity Classification using Convolutional Neural Network*

Spectrograms of each activity are created by taking the Short-Time Fourier Transform [24] of each activity  $S_{21}$  parameter. 5-second windows from these larger 20-second-width spectrograms are shown in Fig. 22. A convolutional neural network is used to classify the four neck-related activities based on their spectrogram images. A CNN is implemented using the MATLAB™ 2017b Deep Learning Toolbox. The network has 2 hidden layers consisting of a convolutional layer and an average pooling layer. The first convolutional layer contains 11 filters and the second layer contains 10 filters. The size of each convolutional filter is 5x5 pixels, taking 1 pixel strides horizontally and vertically across the image. The average pooling layers each have pool size of 2 pixels. These parameters have been determined through a heuristic search. The fully-connected layer has four outputs: chewing, drinking, breathing, and speaking.

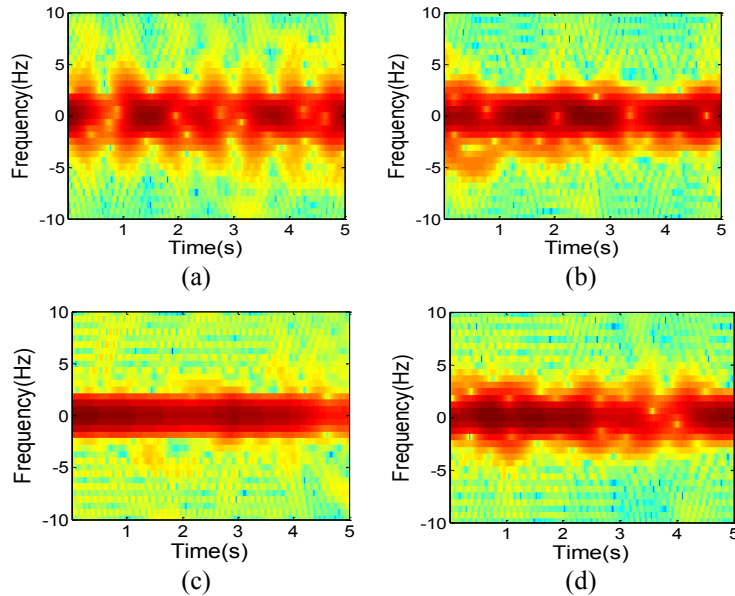


Fig. 22. Spectrograms generated from  $S_{21}$  parameter of (a) chewing, (b) drinking, (c) breathing, and (d) speaking.

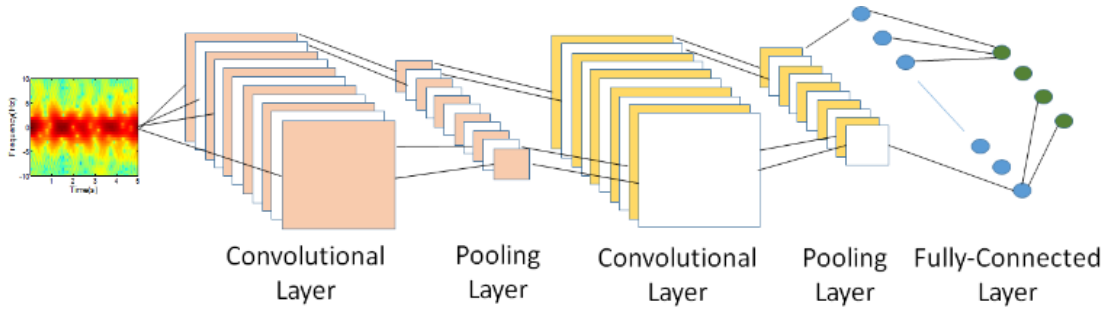


Fig. 23. Architecture of CNN used to classify neck-related activity spectrograms.

10 training spectrograms are randomly sampled from the total 20 second measurement for each trial of each activity for each test subject. The total number of training images is then 10 samples x 4 trials x 4 activities x 6 test subjects = 960 images. 80% of the total measurement data is used to train the network and the remaining 20% is used to validate the network's performance. This validation accuracy is calculated by dividing the number of correct outputs by the total number of outputs, as described in (8), where  $A$  is the accuracy,  $C$  is the correct number of answers, and  $I$  is the number of incorrect answers. All networks have  $0 < A < 1$ , where  $A = 1$  is a perfect network accuracy, and  $A = 0$  is a lousy network accuracy.

$$A = \frac{C}{C + I} \quad (8)$$

For the training, we have two scenarios. The first one is to use data from all subjects for testing and training. In this case, after randomly mixing the whole data, we divide them into training data (80%) and test data (20%). The second case is to use data from four subjects for training and to use data from the remaining two subjects for testing. After training, we calculate the percentage of correctly classified images in the test data, which is the average classification accuracy. For increasing width of the

spectrogram time window, the average classification accuracies are calculated. The result is shown in Fig. 24.

The graphs show that the classification accuracy of 91.4% can be achieved for the first scenario while 84.5% is achieved for the second scenario with a 5- second time window. As the time window increases, so does the classification accuracy. This makes sense since a larger spectrogram image would contain more complex features unique to the activity that caused them, making the job of classifying the images easier for a machine.

The confusion matrix shown in Table 2 summarizes where the CNN was accurate and inaccurate in its results during testing. The horizontal header labels represent which activity the data truly belonged to, and the vertical header labels represent the CNN classification result. Ideally, this table should look like an identity matrix.

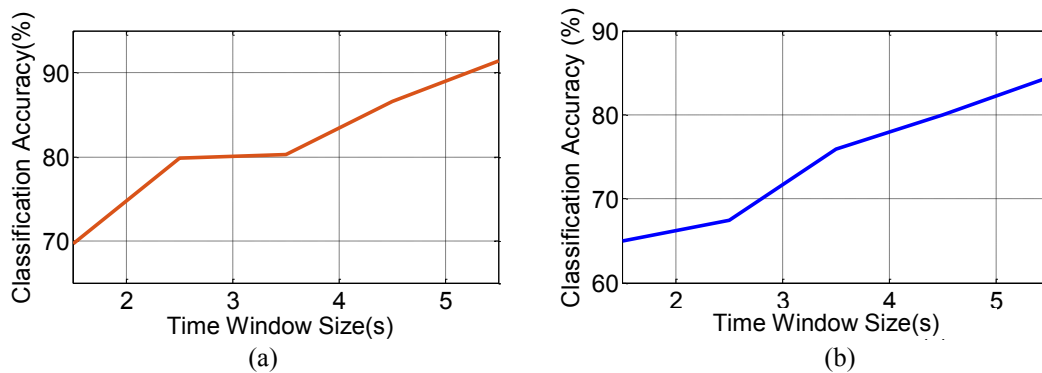


Fig. 24. CNN validation accuracy vs spectrogram window width for (a) the first scenario, and (b) the second scenario.

Table 2. Confusion Matrix for CNN Training.

Est \ True	Chewing	Drinking	Breathing	Speaking
Chewing	81.3%	0%	4.1%	0%
Drinking	0%	91.7%	6.2%	0%
Breathing	10.4%	8.3%	89.7%	0%
Speaking	8.3%	0%	0	100%

## *Conclusion*

In this chapter, the creeping wave S-parameters between two neck-mounted antennas were measured for six test subjects. Each subject acted out chewing, drinking, speaking, and deep breathing activities for 20 seconds. The  $S_{21}$  parameter data was used to generate unique spectrogram images for each activity and test subject. The spectrograms were used as training data for a Convolutional Neural Network in an image classification approach. For the first validation scenario, the CNN was able to classify the activity based on its corresponding spectrogram image with over 90% accuracy for a 5-second time window, and over 74% with a 2-second time window. For the second validation scenario, the respective accuracies fell to 84% for a 5-second window and 65% for a 2-second window.

To improve the neural network accuracy, training with more measurement data from diverse test subjects is crucial. A commercially-available version of this technology would need millions of training sets to be considered reliable, which could be accomplished by recording data as users wear the product throughout its lifetime. Altering the neural network parameters like filter size, number of hidden layers, and pooling size will also have a significant impact on classification accuracy.

## CHAPTER FOUR

### Measurement of Around-Body Creeping Waves Using Wearable Sensor Modules

#### *Introduction*

The development of efficient wireless body-area networks (WBANs) heavily relies on the understanding of radio wave propagation behavior around and near the human body. WBANs may find use in the medical technology field as remote healthcare monitoring systems [1], or in the consumer market as personal activity tracking becomes ever more popular with devices like the Fitbit® and smartwatches. One particular on-body wave mechanism, the creeping wave [14], is of significant concern for WBANs since it is the dominant non-line-of-sight wave mode travelling around the human body.

Around-body creeping waves have been extensively studied in recent years by different research groups [7], [25]-[27]. The attenuation constant of the creeping wave has been identified by a narrowband measurement, while the travelling speed of the wave was determined by wideband measurements. It was also found that the on-body creeping wave signals can be used for continuous-time activity monitoring [7]. For the above narrowband and wideband measurements, a vector network analyzer (VNA) is commonly used and can provide accurate measurement solutions.

However, the large size, heavy weight, and high cost of a VNA makes it prohibitive for any practical field application of wearable technology. Therefore, it is desirable to investigate the capability of miniaturized, affordable, wearable sensors in detecting the

same information that a VNA can capture while making on-body wave propagation measurements.

Two methods for VNA substitution are proposed in this paper. The first is to use the Digi XBee® radio module [28] as a VNA replacement for narrowband scenarios. These radios operate at the ISM 2.4 GHz band with 2 MHz of bandwidth and are designed for affordability, size, and simplicity. The second method is to use the Time Domain PulsON® ultra-wideband (UWB) sensor module [29] to replace the wideband functionality of the VNA. PulsON can generate short time impulses with equivalence of 1.4 GHz bandwidth in the frequency domain.

This chapter is organized as follows: the first section establishes baseline on-body propagation measurements completed with a VNA. The second section explores the performance of the XBee modules as a narrowband VNA replacement, and the third section reports the performance of the PulsON modules as a UWB VNA replacement. The final section concludes with a summary and future work to be done.

### *VNA Baseline Measurements*

To evaluate the proposed new sensor methods, a VNA is first used to take baseline measurements for both narrowband and UWB scenarios: first, narrowband  $S_{21}$  parameters are measured for dynamic around-neck creeping wave propagation; second, the wideband  $S_{21}$  is measured for static around-head creeping wave propagation.

#### *Narrowband Creeping Wave Propagation*

Two quarter-wave monopole antennas are attached to the sides of the neck of a human test subject, shown in Fig. 25. Two test subjects, one male and the other female, are asked to act out an activity for 20 seconds while standing. The activities are chewing,

drinking water, deep breathing, and speaking. As the subject is performing different activities, 2.45 GHz  $S_{21}$  parameters are recorded using the VNA under the continuous time mode.

Fig. 26 shows the  $S_{21}$  magnitude plotted against time for two test subjects. Interestingly, the different activities exhibit different patterns of variation, implying each activity causes different perturbations on the around-neck creeping wave propagation. By applying a convolutional neural network approach, an algorithm was able to classify the activities with more than 90% accuracy.

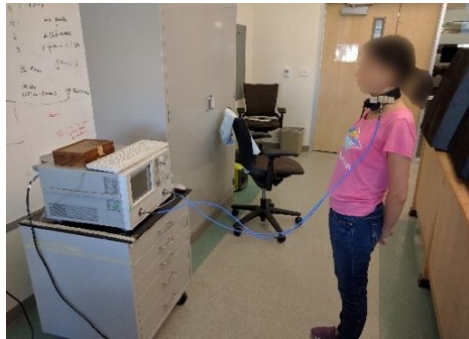


Fig. 25. Narrowband around-neck creeping wave measurement.

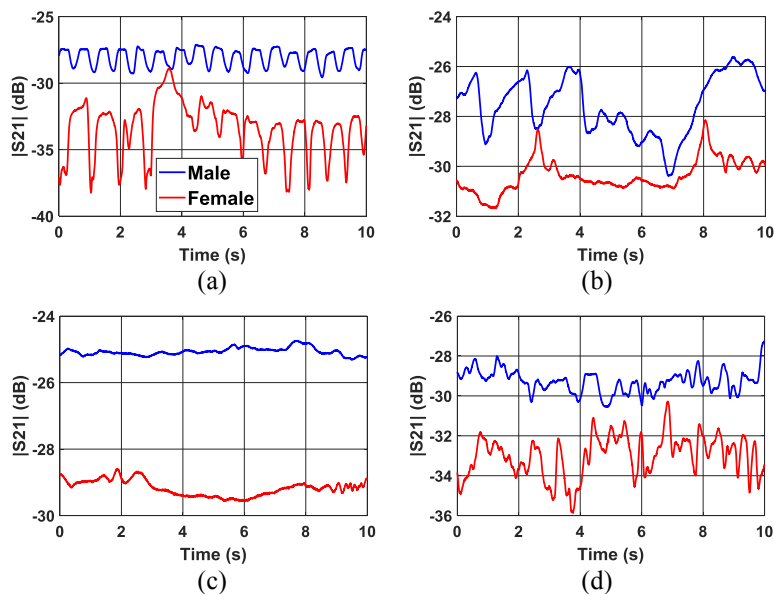


Fig. 26.  $S_{21}$  magnitude curves due to (a) chewing, (b) drinking, (c) deep breathing, and (d) speaking.

### *Ultra-Wideband Creeping Wave Propagation*

Next, the same antennas are moved to the left and right sides of the test subject's head, shown in Fig. 27. Wideband around-head creeping wave measurement.. The VNA is adjusted to measure the around-head creeping wave propagation for a UWB signal from 3.6 to 5 GHz. The test subject does not move for the duration of the experiment.

Fig. 28(a) shows the measured  $S_{21}$  magnitude against frequency. Its time-domain counterpart can be generated by applying the inverse Fourier transform, as shown in Fig. 28(b). The dominant peak arrives at the receiver antenna 1.308 nanoseconds after leaving the transmitter antenna. Since the circumference of the test subject head was measured as 58 cm, the creeping wave path from transmitter to receiver is half of the circumference, or 29 cm. This distance divided by the pulse travel time delay of 1.308 ns results in an apparent creeping wave velocity of  $2.217 \times 10^8$  m/s. It is found that the around-head creeping wave travels slower than the speed of light in free space.



Fig. 27. Wideband around-head creeping wave measurement.

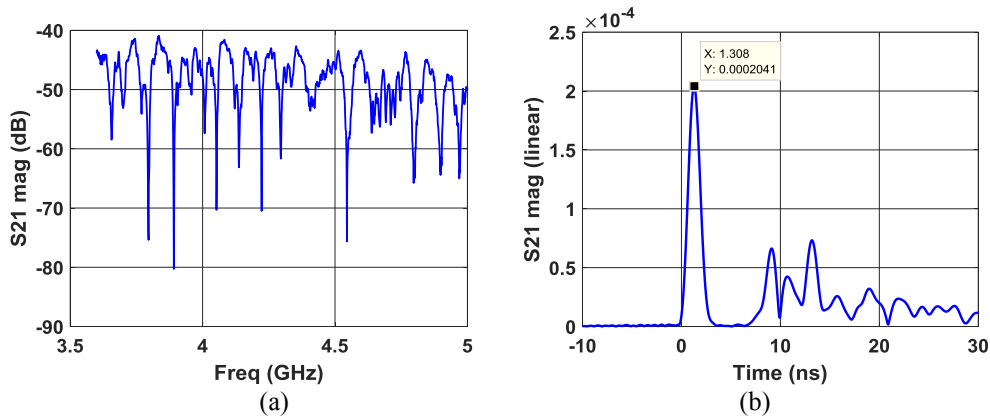


Fig. 28. (a) VNA scan of frequency from 3 to 5 GHz. (b) Time domain representation of UWB frequency scan.

### *Digi XBee Modules*

Digi XBee® radios are small, affordable RF communication modules based on the IEEE 802.15.4 wireless standard. These radios have become a common solution for various projects involving wireless connectivity. The XBees can measure the received signal strength (RSS) of an incoming data packet, which has a value proportional to the S<sub>21</sub> magnitude measured by the VNA. In this work, the Sparkfun® Redboard, based on the Arduino open source hardware, is used to power and control each XBee radio.

### *XBee Scan on Head*

First, two XBee radios are attached to the sides of a human test subject's neck, as shown in Fig. 29. The transmitter (TX) sends the receiver (RX) small data packets at a rate of 100 times per second, which the receiver uses to measure the channel path loss. The RX then sends the value of the RSS to the collector XBee (CO), which logs the data into a nearby computer.

The first activity measured is chewing, which moves the jaw up and down with a certain periodicity. This changing of the environment near the antennas will cause wave

disruptions to occur, affecting the power of the signal read by the RX. The results are plotted in Fig. 30 alongside a VNA scan of the same activity.

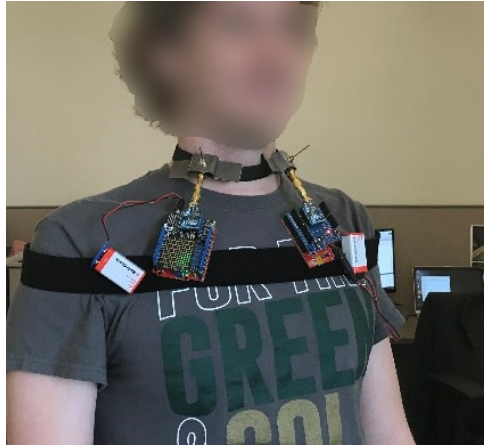


Fig. 29. XBees with antennas attached to test subject's neck.

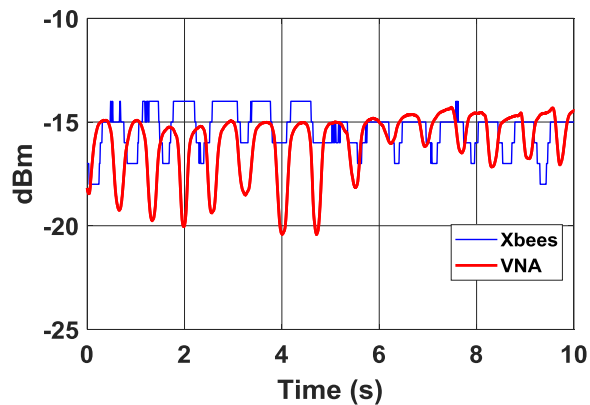


Fig. 30. Measured signal strength in dBm between on-neck antennas for chewing compared between XBees and VNA.

The periodic pattern of the RSS in Fig. 30 shows agreement between the XBee and the VNA scans. The vertical magnitude variation is comparable between both curves, and the overall shape is similar. The sampling rate and quantization values of the XBees are not as highly resolved as those of the VNA, indicated by the unsmooth changes in dBm value for the XBee curve.

### *XBee Scan on Torso*

Next, the XBees are placed on the front and back of a test subject's torso (Fig. 31). The test subject swings his right arm backward and forward with a period of 2 seconds. The XBee results are plotted alongside the VNA scan in Fig. 32. The period is approximately the same for both curves. However, once again, the VNA can measure a much wider range of power levels than the XBees, indicated by the smoother VNA curve reaching minimum values around -70 dBm.

Clearly, there is agreement between the XBees and VNA for the chewing activity. The XBees, while not optimized for power level measurements, are still able to perform decently well at capturing body motion data.

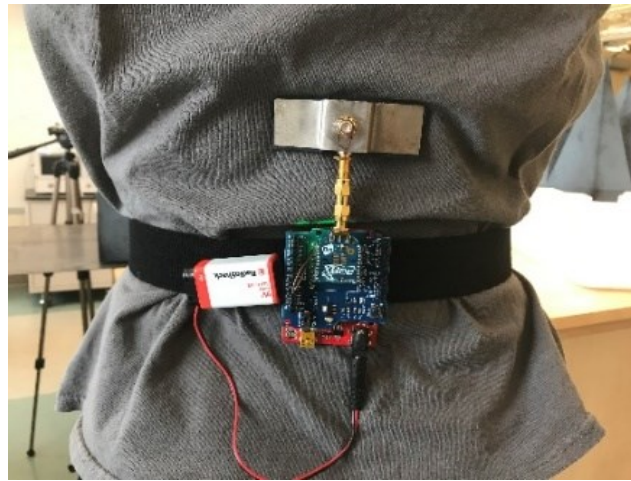


Fig. 31. XBee attachment setup for front of torso—back is similar.

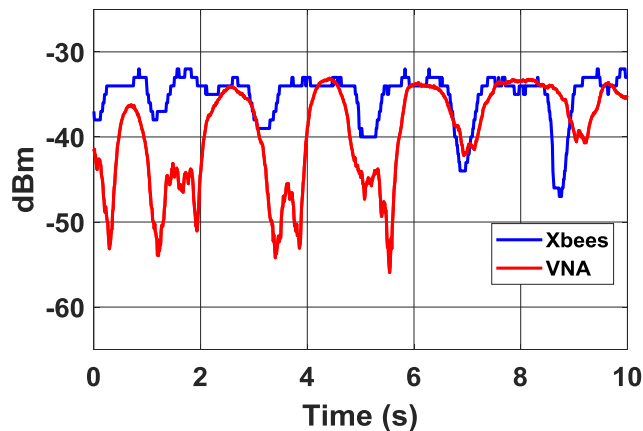


Fig. 32. Measured signal strength in dBm between on-torso antennas for single arm swinging compared between XBees and VNA.

### *Time Domain PulsON Modules*

While the previous section studied narrowband propagation disturbances caused by activities, this section will study the UWB propagation around the head and torso without the test subject moving. Time Domain® produces the ultra-wideband (UWB) PulsON® 440 radar modules, capable of generating a range detection pulse of 7 ns width, which is equivalent to 1.4 GHz of bandwidth from 3.6-5 GHz.

### *UWB Scan on Head*

The PulsON modules are connected to 4-foot long SMA cables with the BroadSpec™ antennas, shown in Fig. 33. Fig. 27 shows how these antennas are connected to the sides of a test subject's head. The transmitter module generates and transmits a short pulse, which the receiver then collects and sends to a laptop PC for processing. The channel impulse response is calculated by de-convolving the received waveform with the transmit waveform template.

This experiment result is compared to the UWB VNA results from the previous section. The phase delay occurring across the human head channel corresponds to time

delay information in the time domain. The inverse Fourier transform of the VNA scan is plotted alongside the PulsON channel impulse response in Fig. 34. Clearly, there is fair agreement between the VNA and PulsON curves.

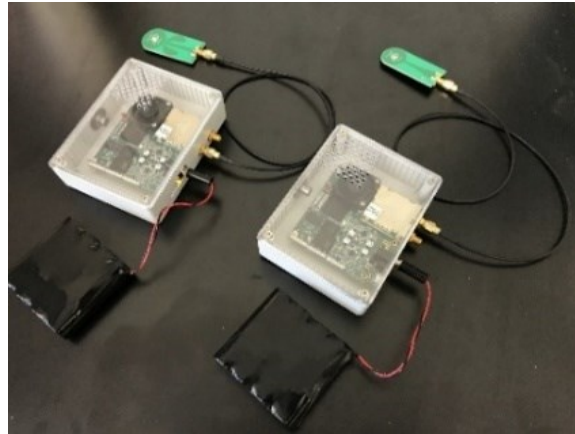


Fig. 33. Time Domain PulsON radar modules with antennas attached with long cables.

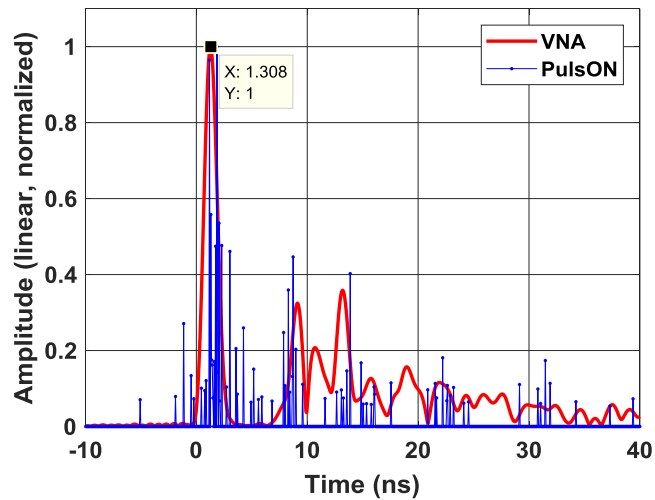


Fig. 34. . Comparison of around-head channel impulse response between PulsON radars and VNA scan.

### *UWB Scan on Torso*

The measurement procedure is repeated with the antennas now placed on the front and back of the test subject's torso, as shown in Fig. 35. The results are shown in Fig. 36.

Once again, there is fair alignment between the PulsON and VNA results. The first impulse response peak for the torso case occurs at 1.587 ns after the reference time. The circumference of the test subject's torso is 82 cm, so the creeping wave path is 41 cm. The creeping wave travel velocity is then  $2.584 \times 10^8$  m/s. There is a much larger spike in amplitude at 9.47 ns after the first spike occurs due to environment multipath effects.



Fig. 35. Antennas attached to front and back of test subject torso.

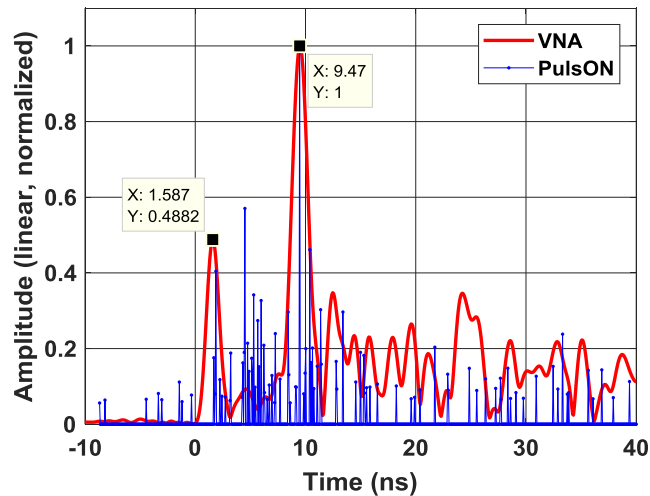


Fig. 36. Comparison of around-torso channel impulse response between PulsON radars and VNA scan.

### *Conclusion*

In this study, both narrowband and wideband on-body creeping wave propagation measurement results were reported. First, a VNA was used to establish the baseline of the research. Then, two different types of wearable sensor modules, the Digi XBees and the Time Domain PulsON sensors, were studied for their ability to replace the network analyzer in a traditional WBAN measurement setup. In both cases, the alternative sensors were able to replicate the results of the VNA to a reasonable degree of accuracy.

Future work in this area should consider developing miniaturized wearable sensor systems meant for applications like personal activity tracking and remote health monitoring.

## CHAPTER FIVE

### Conclusion

#### *Summary*

In summary, the human body can support creeping wave modes which propagate around curved paths at nearly the speed of light. Path loss and phase delay measurements around the head and neck were corroborated with full-wave simulations and a theoretical creeping wave model. The radius of path curvature has a substantial effect on the power decay of a wave propagating around a body part like the head or neck. Material properties of the body part do not affect the wave propagations significantly.

Creeping waves can be used as a sensing mechanism to detect and distinguish daily motions involving the head and neck. The  $S_{21}$  parameter was measured between two neck-worn antennas as test subjects acted out four daily activities. A convolutional neural network was able to classify chewing, drinking, breathing, and speaking with up to 93% accuracy by being fed training images sampled from spectrograms of  $S_{21}$  parameter data.

Lightweight, affordable sensors including the Digi XBee radio and the Time Domain PulsON radar module were used to replace the narrowband and wideband functionality of the VNA, respectively. The narrowband operation of the XBee radios enabled tracking of bodily motions similar to the continuous, narrowband wave operation of the VNA from chapter 2. The PulsON modules were able to recreate the wideband propagation effects of the VNA by measuring the short pulse time delay around the head and torso.

### *Future Work*

Future work regarding WBANs and wearable antennas must focus on practical field applications that enable users to comfortably and easily interface with their wearable wireless systems. Design of small, lightweight antennas for wearable purposes is critical to achieve this goal. Potential solution candidates for this problem may include textile antennas integrated into clothing articles, jewelry dielectric resonator antennas, and antennas integrated into commonly worn items like glasses, headphones, and hats.

Additionally, real-time data classification must be realized for WBANs to be useful to any user. The research presented in this thesis relied on post-processing of measurement data in MATLAB for all experiments. WBAN systems need to be streamlined so the relevant user's health or activity information is processed automatically and delivered to the intended recipient in real time. Data processing could occur within the wearable system itself, or on a remote computer which receives the raw physiological data from the wearable sensors.

Finally, RF interference concerns must be addressed. Radiation emanating from the WBAN user's body must propagate with low enough power to not interfere with surrounding wireless signals of similar frequencies; if the WBAN operates over ISM band spectra, nearby Bluetooth or Wifi systems may be affected. Likewise, these off-body ISM systems may interfere with the WBAN, since their transmission power is designed to be great enough to propagate over several tens or hundreds of feet. Security protocol must also be addressed as radiation from the WBAN user's body will not likely be permitted through airport X-Ray machines or near RF-sensitive equipment.

## BIBLIOGRAPHY

- [1] J.M. Smith, "The doctor will see you ALWAYS," *IEEE Spectrum*, vol. 48 no. 10, pp. 57-62, Oct. 2011.
- [2] S. Patel *et al.*, "Home monitoring of patients with Parkinson's disease via wearable technology and a web-based application," in *2010 Annual International Conf. IEEE Engineering Medicine Biology Society*, Buenos Aires, Argentina, pp. 4411-4414.
- [3] G. Fenu and G. Steri, "Two methods for body parameter analysis using body sensor networks," in *Int. Conf. Ultra Modern Telecommunications and Workshops*, St. Petersburg, Russia, 2009, pp. 1-5.
- [4] F. Huo, E. Hendriks, P. Paclik, A.H.J. Oomes, "Markerless human motion capture and pose recognition," in *Proc. 10th IEEE Workshop on Image Analysis for Multimedia Interactive Services*, London, U.K., 2009, pp. 13-16.
- [5] S. Wang and G. Zhou, "A review on radio based activity recognition," *Digit. Commun. Netw.*, vol. 1, no.1, pp. 20-29, Feb. 2015.
- [6] Y. Li *et al.*, "Human Activity Classification Based on Dynamic Time Warping of an On-Body Creeping Wave Signal," *IEEE Trans. Antennas Propag.*, vol. 64, no. 11, pp. 4901-4905, Nov. 2016.
- [7] Y. Kim and Y. Li, "Human Activity Classification with Transmission and Reflection Coefficients of On-Body Antennas Through Deep Convolutional Neural Networks," *IEEE Trans. Antennas Propag.*, vol. 65, no. 5, pp. 2764-2768, May 2017.
- [8] K. Yatani and K. N. Truong, "BodyScope: A Wearable Acoustic Sensor for Activity Recognition," in *Proc. 2012 ACM Conf. Ubiquitous Computing (UbiComp '12)*, Pittsburgh, PA, pp. 341-350.
- [9] J. Cheng *et al.*, "Designing Sensitive Wearable Capacitive Sensors for Activity Recognition," *IEEE Sensors Journal*, vol. 13, no. 10, pp. 3935-3947, Oct. 2013.
- [10] B. Fang, N. D. Lane, F. Kawsar, "Headscan: A Wearable System for Radio-based Sensing of Head and Mouth-related Activities," in *15th ACM/IEEE Int. Conf. Information Processing Sensor Networks (IPSN)*, Vienna, Austria, 2016, pp. 1-12.
- [11] B. Xu, Y. Li, and Y. Kim, "Classification of finger movements based on reflection coefficient variations of a body worn electrically small antenna," *IEEE Antennas Wireless Propag. Lett.*, vol.16, pp. 1812-1815, Mar. 2017.

- [12] P.S. Hall *et al.*, “Antenna and propagations for on-body communication systems,” *IEEE Antennas Propag. Mag.*, vol. 49, no. 3, pp. 41–58, Jun. 2007.
- [13] J. Ryckaert *et al.*, “Channel model for wireless communication around human body,” *IEE Electron. Lett.*, vol. 40, no. 9, pp. 543–544, 2004.
- [14] D. Xue, B. Garner, Y. Li, “Investigation of short-range, broadband, on-body electromagnetic wave propagations,” *IET Microwaves, Antennas, and Propagation.*, pp. 1-7, April 2016.
- [15] D. Xue., Garner, B.A., Li, Y. “Extraction of on-body creeping wave mechanisms using the ESPRIT algorithm”, *Microw. Opt. Technol. Lett.*, vol. 57, no. 4, pp. 868–871, Feb 2015.
- [16] J. R. Wait, “The ancient and modern history of EM ground-wave propagation,” *IEEE Antennas Propag. Mag.*, vol. 40, no. 5, pp. 7–24, Oct 1998.
- [17] D. E. Foreman and D. F. Sedivec, “Experimental observation of the creeping-wave phenomenon in backscatter using a short-pulse radar system,” *Proc. of the IEEE*, vol 53, issue 8, pp. 1102-1104, Aug. 1965.
- [18] T. Alves, B. Poussot, J. Laheurte, “Analytical Propagation Modeling of BAN Channels Based on the Creeping Wave Theory,” *IEEE Trans. Antenna Propag.*, vol. 59, no. 4, pp. 1269-1274, April 2011.
- [19] FEKO [Online]. Available: <https://www.feko.info>.
- [20] Takashi Hikage et al, “Whole-body averaged SAR measurements using cylindrical-external field scanning for 2 GHz plane wave irradiation of human models,” in *7th European Conference on Antennas and Propagation (EuCAP)*, Gothenburg, Sweden, 2013, pp. 1773-1774.
- [21] Wei Xia et al, “Performance of an implanted cavity slot antenna embedded in the human arm,” *IEEE Trans. Antennas Propag.* vol. 57, no. 4, pp. 894-899, April 2009.
- [22] R. Roy, A. Paulraj, and T. Kailath, “ESPRIT—A subspace rotation approach to estimation of parameters of cissoids in noise,” *IEEE Trans Acoust Speech Signal Process*, vol. 34, pp. 1340–1342, 1986.
- [23] Convolutional Neural Networks [Online]. Available: <https://www.mathworks.com/discovery/convolutional-neural-network.html>.
- [24] V. Chen and H. Ling, *Time-Frequency Transforms for Radar Imaging and Signal Analysis*, Artech House, 2002.

- [25] D. Bresnahan and Y. Li, "Investigation of creeping wave propagation around the human head at ISM frequencies," *IEEE Antennas Wireless Propag. Lett.*, vol. 16, pp. 2767-2770, Aug. 2017.
- [26] J. Chen, Y. Ye, K. Pahlavan, "UWB characteristics of creeping wave for RF localization around the human body," in *Proc. 23<sup>rd</sup> International Symp. Personal Indoor and Mobile Radio Communications*, Sydney, Australia, 2012, pp. 1290-1294.
- [27] T. Kumpuniemi *et al.*, "Path loss modeling for UWB creeping waves around human body," in *Proc. 11<sup>th</sup> Int. Symp. Medical Information Communication Technology*, Lisbon, Portugal, 2017, pp. 44-48.
- [28] Digi XBee [Online]. Available: <https://www.digi.com/products/xbee-rf-solutions/2-4-ghz-modules/xbee-802-15-4>.
- [29] Time Domain PulsON 440 [Online]. Available: <http://www.timedomain.com/products/pulson-440/>.